relative to that for He I.[2a] Although the atomic Pt 5d cross section (29.5 Mb at 21.2 eV and 31.3 Mb at 40.8 eV)[50] does not increase as much as most d cross sections from He I to He II photons, the large decrease in the C 2p cross section (6.1 Mb at 21.2 eV and 1.9 Mb at 40.8 eV) suggests that there should still be very large changes (up to a factor of 3) in He II:He I intensity ratios for peaks arising from orbitals of such widely different Pt 5d characters (Table II). However, recent results [e.g. for bis(π-allyl)-nickel],[48] in which the Ni 3d cross section increases dramatically from He I to He II photons, show that He II:He I ratios cannot be used confidently for assigning metal d peaks, and there are at least two possible causes of the "anomalous" He II:He I ratios for our compounds. First, resonance effects (such as "shape" resonances) recently seen in synchrotron radiation studies in many molecules[49] can radically change relative intensities from those of the atomic Gelius treatment.[31] Second, changes in shape of the Pt 5d cross section as a function of photon energy from the atomic behavior[50] could give He II 5dπ intensities radically different from those expected on the atomic model. There has been considerable experimental[51] and theoretical[52] evidence that the shape of heavy-metal 5d cross sections are dependent on the chemical and physical state of the heavy metal. For example, the Pb $5d_{5/2}$ cross-section maximum shifts from 37-eV kinetic energy for a thin Pb film on a Ni(110) surface[51b] to ~22 eV for bulk Pb. The shape of the 5d cross section is a function of the outgoing photoelectron f-wave phase shift, which is sensitive to the nuclear potential at the heavy metal.[52] Thus, if the maximum of the Pt 5d cross section shifts from ~25-eV kinetic energy in the atomic case[50] to ~10-15 eV in these Pt compounds, our anomalous He II:He I ratios could be readily rationalized. Synchrotron radiation studies are now required to confirm which of these two mechanisms is most important, but the second one seems more probable because all intensities remain relatively similar in He I and He II spectra.

(50) Lindau, I.; Yeh, J. J. *At. Nucl. Data Tables* **1987**, *32*, 1.
(51) (a) Bice, J. E.; Tan, K. H.; Bancroft, G. M.; Yates, B. W.; Tse, J. S. *J. Chem. Phys.* **1987**, *87*, 821. (b) Guertler, K.; Tan, K. H.; Bancroft, G. M.; Norton, P. R. *Phys. Rev. B.* **1987**, *35*, 6024.
(52) Tambe, B. R.; Manson, S. T. *Phys. Rev.* **1984**, *30*, 256.

Conclusions

In the complexes $CpPtMe_3$ and Cp^*PtMe_3, the ionization energies of the filled valence molecular orbitals follow the order Pt 5d < Pt–Me < Cp–Pt. There is strong interaction between the platinum d_{xz} and d_{yz} orbitals with both the Cp e_1'' π and the Me_3 e σ sets. The conclusions based on our photoelectron study indicate that very effective covalent bonding is present in the high oxidation states of the heavy-transition-metal complexes.

Acknowledgment. D.S.Y., G.M.B., and R.J.P. thank the NSERC (Canada) for financial support and J. D. Bozek for help with the computer fitting of the spectra. D.S.Y. wishes to thank the University of Western Ontario for a visa bursary, and S.D.M. thanks Drs. Roger H. Cayton and Michael R. Green for their helpful discussions on the calculational aspects of this project.

Contribution from the Department of Chemistry, Stanford University, Stanford, California 94305

Transverse and Longitudinal Zeeman Effect on $[PPh_4][FeCl_4]$: Assignment of the Ligand Field Transitions and the Origin of the $^6A_1$ Ground-State Zero-Field Splitting

Joseph C. Deaton, Matthew S. Gebhard, and Edward I. Solomon*

Received August 5, 1988

The spin-forbidden ligand field transitions of the high-spin ferric site in $[PPh_4][FeCl_4]$ (D_{2d} symmetry) are definitively assigned through polarized single-crystal absorption, transverse Zeeman, and magnetic circular dichroism spectroscopies. A key feature of the magnetooptical experiments is the use of high magnetic field and low temperature to selectively populate the $M = {}^5/_2$ sublevel of the $^6A_1$ ground state. The marked dependence of polarized intensity upon ground spin substate is due to the involvement of spin as well as orbital vector coupling coefficients in the selection rules derived for the spin–orbit intensity gaining mechanism. From the observed $^4T_1$ axial splitting it is found that Griffith's theory relating the $^6A_1$ ground-state zero-field splitting, D, to spin–orbit interactions with $^4T_1$ excited states predicts the wrong sign of D. A modification to this theory is presented that includes the effect of anisotropic covalency in the σ-antibonding orbitals on the spin–orbit coupling matrix elements. The effect of covalency is further probed through the inability of the three-parameter ligand field theory to account for the experimental ligand field transition energies.

Introduction

A wide variety of proteins and enzymes contain ferric active sites that have high-spin d^5 electronic configurations. As these Fe^{3+} centers play a key role in biological processes, it is of importance to relate the spectral features of these active sites to their geometric and electronic structure.

The ultraviolet and visible absorption spectra of ferric complexes are dominated by intense, spin-allowed ligand to metal charge-transfer (CT) transitions. The ligand field (LF), or d–d, transitions have not been observed in proteins as they are all spin-forbidden and thus very weak. Energies for the LF transitions are predicted by the Tanabe–Sugano matrices.[1] In tetrahedral symmetry, the ground state is $^6A_1(t_2^3e^2)$ and the low-lying excited states in order of increasing energy are $^4T_1{}^a(t_2^2e^3)$, $^4T_2{}^a(t_2^2e^3)$, $^4A_1(t_2^3e^2)$, $^4E^a(t_2^3e^2)$, $^4T_2{}^b(t_2^3e^2)$, and $^4E^b(t_2^3e^2)$.

The $^6A_1$ ground state for many Fe^{3+}-containing proteins has been probed by EPR spectroscopy.[2] The EPR spectrum for an $S = {}^5/_2$ ion in axial site symmetry is described by the spin Hamiltonian[3]

$$\mathcal{H} = g\beta H\cdot S + (a/6)(S_z^4 + S_x^4 + S_y^4) + DS_z^2 + (F/180)(S_z^4 - (30S(S+1) + 25)S_z^2) \quad (1)$$

The first term in eq 1 is the Zeeman splitting. Since there are no sextet excited states within the ligand field manifold available for spin–orbit (SO) coupling interactions, the g values are predicted by ligand field theory to be isotropic with the spin-only value of 2.0023. The parameter a is the zero-field splitting (ZFS) of $^6A_1$ in cubic symmetry. As this term results from higher order interactions in spin–orbit coupling and cubic ligand field, it is predicted to be very small. If the symmetry is less than cubic, the axial ZFS parameter, D, will be nonzero and lift the degeneracy of the $M = \pm{}^1/_2$, $\pm{}^3/_2$, and $\pm{}^5/_2$ spin states by $2D$ and $4D$, respectively. The parameter F describes a higher order term in the axial distortion and is very small.

The goal of this study is to provide a basic understanding of the information content of these spectral features through a detailed single-crystal study of $[PPh_4][FeCl_4]$. In this compound the $FeCl_4^-$ complex occupies a site of rigorous S_4 crystallographic symmetry, with effective D_{2d} molecular symmetry.[4] The D_{2d}

(1) Tanabe, Y.; Sugano, S. *J. Phys. Soc. Jpn.* **1954**, *9*, 753.
(2) Smith, T. D.; Pilbrow, J. R. *Biol. Magn. Reson.* **1980**, *2*, 85.
(3) Bleaney, B.; Trenam, R. S. *Proc. R. Soc. London* **1954**, *A223*, 1.

0020-1669/89/1328-0877$01.50/0

compressed Cl–Fe–Cl angle bisected by the S_4 axis is 114.6° at room temperature. The ground state is studied by single-crystal EPR, and the ligand field excited states are examined by single-crystal polarized absorption, transverse Zeeman, and longitudinal Zeeman (MCD) experiments.

There are three critical reasons for a rigorous examination of the LF excited states. First, according to Griffith[5] the $^4T_1$ splitting in axial symmetry is the origin of the ground state ZFS, D, through a second-order SO coupling interaction. However, this theory has not been tested experimentally since there have been no assignments of the $^4T_1$ orbital partners in low symmetry for any Fe^{3+} complex. Second, analysis of the LF many-electron excited-state energies, including low-symmetry effects, can provide the energy ordering of the one-electron d orbitals and, thus, the relative strengths of covalent antibonding interactions with the 3p orbitals on the ligands. Finally, the electron repulsion parameters obtained from a ligand field analysis using the Tanabe–Sugano matrices provide a general probe of covalency at the ferric site.

There have been very few studies[6,7] of the LF excited states in Fe^{3+} compounds. $[AsPh_4][FeCl_4]$ has been examined[8] in the past by polarized absorption, and the bands were assigned by a fit of their energies to the Tanabe–Sugano matrices.[1] However, as will be clear from this study, the complexity of the ferric tetrachloride spectrum requires a more direct method for experimentally assigning the transitions, based on behavior predicted by group theory. Selection rules for polarized absorption and transverse and longitudinal Zeeman experiments are derived in D_{2d} symmetry through application of the irreducible tensor method[9] to the spin–orbit coupling mechanisms for intensity in the $^6A_1 \rightarrow {}^4h$ (h = A_2, A_1, E, T_2, T_1) transitions. The key feature of our magnetooptical experiments is the use of high field and low temperature to selectively populate the $M = -^5/_2$ Zeeman sublevel of the ground state. In the transverse Zeeman effect (TZE), the absorption of plane-polarized light is measured with the magnetic field parallel to the tetragonal, S_4, crystal axis and perpendicular to the propagation direction of the light. Complimentary selection rules are provided by the longitudinal Zeeman effect, or magnetic circular dichroism (MCD), experiment in which the differential absorption of left and right circularly polarized light is measured with the propagation direction of the light parallel to both the field and the tetragonal axis. The spectral studies reported here on $[PPh_4][FeCl_4]$ build on those of McCarthy and Vala[8] and represent the first experimentally definitive assignment of an Fe^{3+} LF spectrum, including the axial splitting of $^4T_1$[a]. These assignments are used to determine the origin of the ZFS of the $^6A_1$ ground state and the effect of covalent interactions on the applicability of the three-parameter (Dq, B, C) ligand field theory to high-spin ferric complexes. Finally, these studies provide an electronic structure reference for parallel spectral studies of models for the active site of oxidized rubredoxin,[10-12] an FeS_4 center involved in electron-transfer reactions in biological systems.

Experimental Methods

Crystals[4] of $[PPh_4][FeCl_4]$ were grown by a solvent diffusion technique in which absolute ethanol was layered on top of a saturated solution of the compound in acetone. The gallium(III) tetrachloride analogue is isomorphous and isostructural[13] and is used as a host lattice for experiments requiring dilute concentrations of ferric tetrachloride. Doped crystals of $[PPh_4][(Ga:Fe)Cl_4]$ were grown by the same method after mixing desired proportions of the Ga and Fe compounds in acetone. Crystals were oriented with a polarizing microscope. For EPR, doped crystals (0.1% Fe) were mounted with grease to the end of a quartz rod that fit snugly in an EPR tube. For optical experiments, crystals were mounted on quartz windows with epoxy or grease around the edges and then masked off with black electrical tape. Crystals could be polished to a desired thickness after first mounting them on a quartz window with a low-melting organic compound or epoxy. The crystals were then polished with a 9 μm grit polishing paper or with a homemade polishing apparatus.

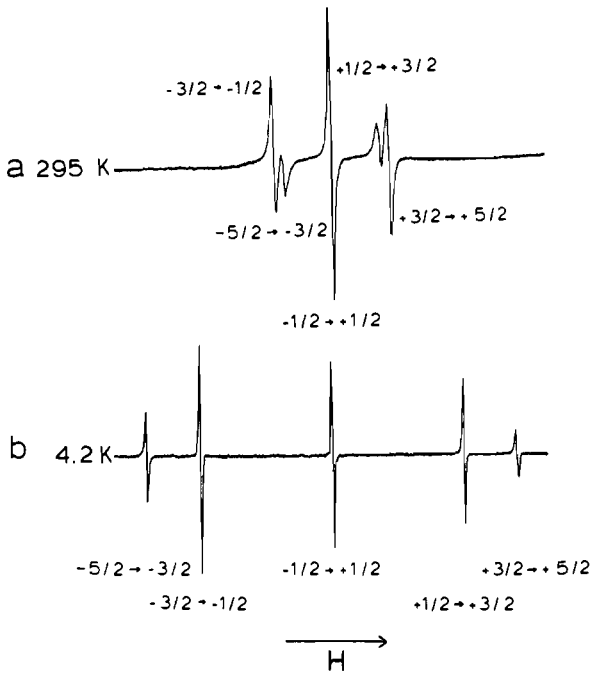

Figure 1. EPR spectra of 0.1% $[PPh_4][FeCl_4]$ with H parallel to the S_4 crystal axis: (a) room temperature, 9.510 GHz, 2-mW microwave power, and 4-G modulation; (b) 4.2 K, 9.510 GHz, 10-μW microwave power, and 2-G modulation.

Polarized absorption spectra were measured on a McPherson RS-10 double-beam spectrophotometer described previously,[14] but with upgraded electronics. A pair of Glan-Taylor polarizers matched from 200 nm to 2.5 μm were used to polarize the sample and reference beams. Three gratings blazed at 3000 Å, 7500 Å, and 1.25 μm were used to cover the different spectral regions. An extended S-20 photomultiplier tube covered the region from 2200 to 8000 Å and a dry-ice-cooled S-1 tube covered 5000 Å to 1 μm. A Joule-Thompson cooled PbS detector was used from 8500 Å to 2.5 μm. The last detector required use of a chopped (560 Hz) light source and a lock-in amplifier. The light sources were a tungsten–halogen lamp for the visible and near-IR regions and a deuterium lamp for the near-UV region. Variable-temperature absorption experiments from 300 to 2 K were done with a Janis Super-Vari Temp Dewar. For the transverse Zeeman effect experiments, an Oxford Instruments SM4 superconducting magnet was placed between the light source and the McPherson monochromator. In the present application, changes in intensity of broad bands are of interest; therefore, it was necessary to select detector and grating combinations that gave the least wavelength-dependent base line in single-beam mode. The SM4 magnet was also configured with a JASCO 500-C spectropolarimeter as described previously[15] for MCD. EPR spectra were taken on a Bruker ER 220D spectrometer with X-band (9 GHz) and Q-band (34 GHz) microwave systems. For X-band experiments, temperatures from 4.2 to 300 K were achieved with an Air Products LTR3 liquid helium refrigerator, while for Q-band, temperatures down to 100 K were achieved with a Bruker flow system using cold nitrogen gas. The precise orientation of the axial crystals relative to the magnetic field was determined by ob-

(4) Zaslow, B.; Rundle, R. E. *J. Phys. Chem.* **1957**, *61*, 490. Note: While the crystal structure is for $[AsPh_4][FeCl_4]$, the PPh_4^+ salt was chosen for this study because the larger crystals of this salt did not crack at low temperature. Comparative studies of the EPR and LF spectra indicate that the D_{2d} distortions of $FeCl_4^-$ in both salts are practically identical at temperatures from 300 to 2 K.
(5) Griffith, J. S. *The Theory of the Transition-Metal Ions*; Cambridge University Press: New York, 1964.
(6) Neuenschwander, K.; Gudel, H. U.; Collingwood, J. C.; Schatz, P. N.; *Inorg. Chem.* **1983**, *22*, 1712.
(7) Holt, S.; Dingle, R. *Acta Chem. Scand.* **1968**, *22*, 1091.
(8) Vala, M. T.; McCarthy, P. J. *Spectrochim. Acta* **1970**, *26A*, 2183.
(9) Griffith, J. S. *The Irreducible Tensor Method for Molecular Symmetry Groups*; Prentice Hall: Englewood Cliffs, NJ, 1962.
(10) Miller, M.; Lee, J. F.; Koch, S. A.; Fikar, R. *Inorg. Chem.* **1982**, *21*, 4105.
(11) Lovenberg, W. In *Iron-Sulfur Proteins*; Eaton, W. A., Ed.; Academic Press: New York, 1973; Vol. II, pp 131–162.
(12) Deaton, J. C.; Gebhard, M. S.; Koch, S. A.; Millar, M.; Solomon, E. I. *J. Am. Chem. Soc.* **1988**, *110*, 6241.
(13) Scaife, D. E. *Aust. J. Chem.* **1970**, *23*, 2205.
(14) Wilson, R. B.; Solomon, E. I. *Inorg. Chem.* **1978**, *17*, 1729.
(15) Allendorf, M. D.; Spira, D. J.; Solomon, E. I. *Proc. Natl. Acad. Sci. U.S.A.* **1985**, *82*, 3063.

Table I. Zero-Field Splitting Parameters for 0.1% $[PPh_4][(Ga:Fe)Cl_4]$ at Several Temperatures

T, K	D, cm^{-1}	$a + 2F/3$, 10^{-4} cm^{-1}	T, K	D, cm^{-1}	$a + 2F/3$, 10^{-4} cm^{-1}
295	−0.0109	+75.6	120	−0.0316	+86.6
185	−0.0253	+84.7	4.2	−0.0419	+89.9

servation of the turning points in the angular dependence of the spectrum.

Results

A. Electron Paramagnetic Resonance. The room-temperature EPR spectrum of a single crystal of $[PPh_4][(Ga:Fe)Cl_4]$ (0.1% nominal Fe concentration) with the S_4 axis aligned parallel to the magnetic field is given in Figure 1a. For $S = {}^5/_2$, there are five allowed $\Delta M = \pm 1$ transitions. Since five transitions are observed, the ZFS parameters, D and a, must be less than the Zeeman splitting, $g\beta H$ (about 0.3 cm^{-1} in this X-band experiment). The magnetic dipole matrix elements[16] for the allowed transitions predict an intensity pattern of 8:5:9:5:8 for the ${}^{-3}/_2 \leftrightarrow {}^{-1}/_2$, ${}^{-5}/_2 \leftrightarrow {}^{-3}/_2$, ${}^{-1}/_2 \leftrightarrow {}^{+1}/_2$, ${}^{+3}/_2 \leftrightarrow {}^{+5}/_2$, and ${}^{+1}/_2 \leftrightarrow {}^{+3}/_2$ transitions, respectively. This pattern is seen in Figure 1a. However, ${}^{-3}/_2 \leftrightarrow {}^{-1}/_2$ is indistinguishable from ${}^{+1}/_2 \leftrightarrow {}^{+3}/_2$, and ${}^{-5}/_2 \leftrightarrow {}^{-3}/_2$ from ${}^{+3}/_2 \leftrightarrow {}^{+5}/_2$. Therefore, only the magnitude of D and the quantity $a + 2F/3$ may be obtained from fitting the room-temperature spectrum to perturbation expressions for the spin Hamiltonian[3] of eq 1. To obtain unambiguous assignment of the transitions and hence the signs of the ZFS parameters, it is necessary to perturb the intensity pattern through the use of low temperature to introduce Boltzmann population factors.[17]

Figure 1b presents the spectrum at 4.2 K. As the temperature is lowered from 295 to 4.2 K, the magnetic field separation increases between the outer lines and the central ${}^{-1}/_2 \leftrightarrow {}^{+1}/_2$ transition. This effect is continuous and reversible with temperature, and axial symmetry is maintained throughout the temperature range studied. Note that at low temperature the $\pm{}^3/_2 \leftrightarrow \pm{}^5/_2$ transitions become the outermost pair of lines. The increase in magnetic field separation between the spectral lines indicates an increase in the magnitude of D. From this it may be inferred that there is an increase in the D_{2d} distortion of $FeCl_4^-$ caused by a contraction of the lattice as the temperature is lowered. Effects of this temperature-dependent lattice distortion are also observed in the ligand field and charge-transfer spectra (vide infra).

In the 4.2 K spectrum the low-field lines are more intense than the corresponding high-field lines. This arises because the $M = {}^{-5}/_2$ state is most populated for $g\beta H > D$. Thus, the specific spin states may be assigned and these are given below each transition in Figure 1b. This order of the transitions indicates that D is negative. Bleaney and Trenam's perturbation expressions[3] have been solved for D and the quantity $a + 2F/3$, which are given for several temperatures in Table I. Q-Band (34-GHz) experiments were further pursued in order to accurately determine $g_z = 2.0148 \pm 0.0008$ directly from the ${}^{-1}/_2 \leftrightarrow {}^{+1}/_2$ transition when the field is parallel to the S_4 axis. $g_{x,y}$ is found to be 2.0125 ± 0.0015 after using perturbation expressions to estimate off-diagonal terms in D when the S_4 axis is perpendicular to the magnetic field. The parameters a and F were obtained independently from the rotational dependence of the EPR spectrum ($a = +85 \times 10^{-4}$ cm^{-1}, $F = -3 \times 10^{-4}$ cm^{-1} at 185 K).

B. Ligand Field Transitions. The single-crystal absorption spectrum of the ligand field transitions in $[PPh_4][FeCl_4]$ at 6 K is shown in Figure 2 for light polarized parallel (z) and perpendicular (x,y) to the S_4 axis. The spectrum is divided into three regions as indicated, and the bands are labeled A–G. Distinct peaks corresponding to C and E are not evident in the absorption spectrum but are required by the MCD experiments described below.

Region I. The absorption spectrum as a function of temperature for this spectral region is presented in Figure 3a for z polarization and in Figure 3b for x,y polarization. The lowest energy band

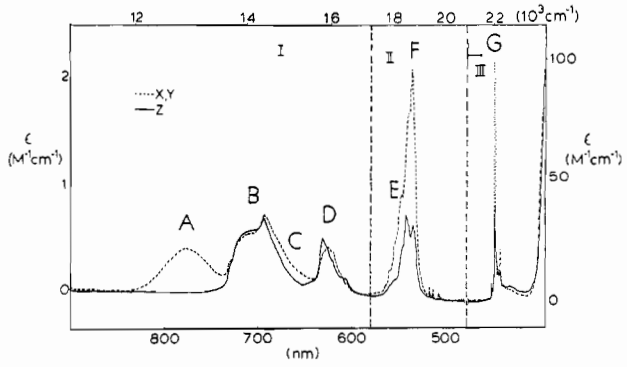

Figure 2. Polarized absorption spectra of $[PPh_4][FeCl_4]$ at 6 K. For the 500–800-nm region, the crystal thickness was 1 mm and the ϵ scale at the left applies. For the 400–500-nm region, a 10% $[PPh_4][(Ga:Fe)Cl_4]$ crystal was used and the right ϵ scale applies.

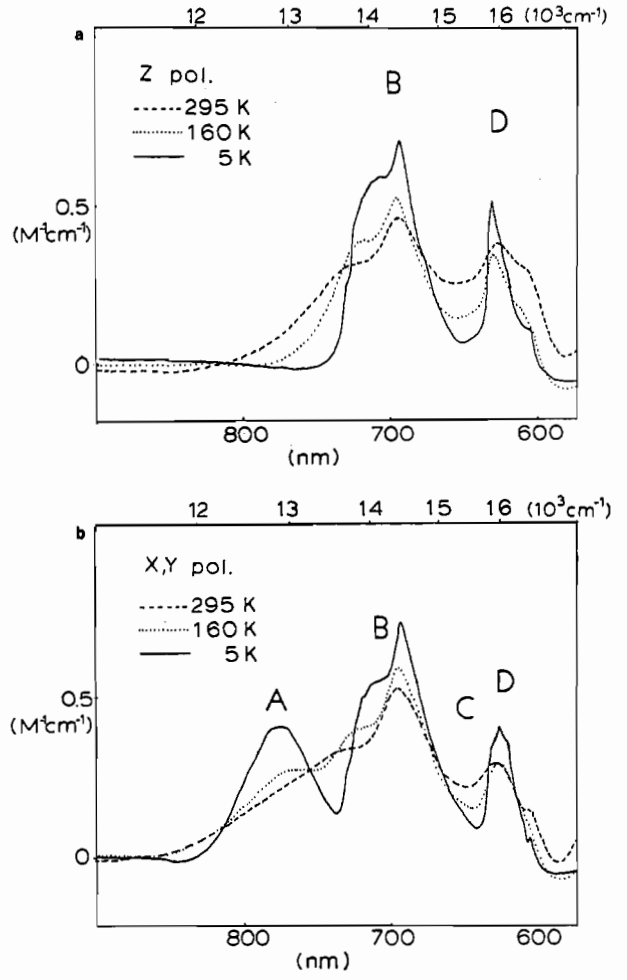

Figure 3. Region I polarized absorption spectra of $[PPh_4][FeCl_4]$ (2.1 mm thick crystal): (a) z-polarized spectrum; (b) x,y-polarized spectrum.

(A) is notable for its pure x,y polarization, which is clearly seen in the 6 K spectrum (this behavior was not observed by earlier workers,[8] who recorded spectra at higher temperatures). The temperature-dependent D_{2d} distortion apparent from the EPR results correlates with the increase in splitting between bands A and B as the temperature is lowered.

Further insight into the assignment of the bands in region I can be achieved in TZE experiments, where the combination of high magnetic field and low temperature are used to selectively populate only the $M = {}^{-5}/_2$ sublevel of the ground state. Figure 4 presents the intensity changes in the polarized absorption spectra at 2 K when a 5 T magnetic field is applied parallel to the S_4 axis. In z polarization (Figure 4a), both bands B and D show approximately a 50% increase in intensity. A striking effect is observed in the x,y polarization (Figure 4b), where bands B and

(16) Meyer, P. H. E. *Physica* **1951**, *17*, 899.
(17) Low, W. *Phys. Rev.* **1957**, *105*, 792.

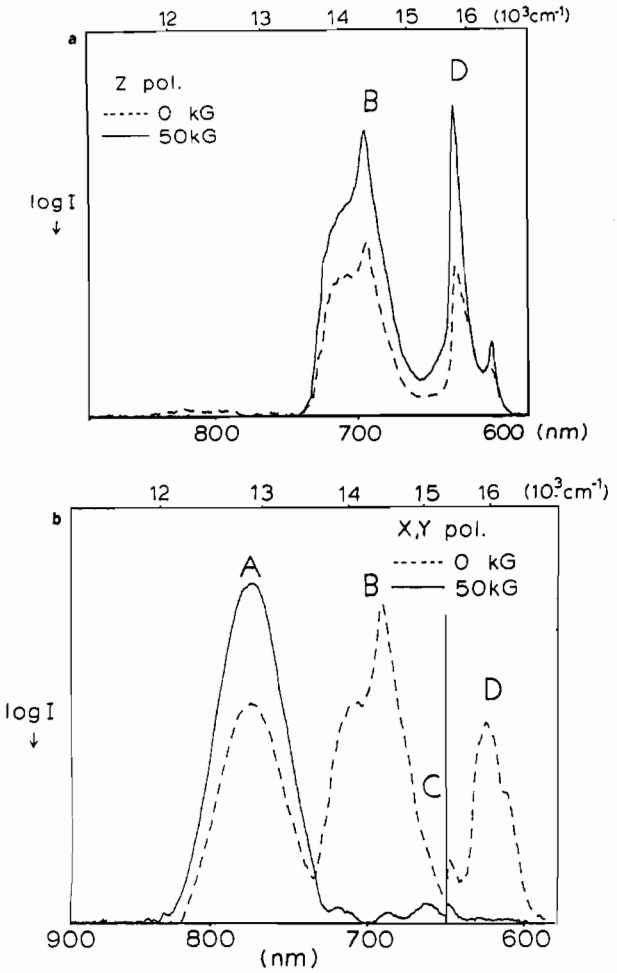

Figure 4. Transverse Zeeman effect for region I at 2 K with no field and a 50-kG magnetic field applied parallel to the S_4 crystal axis of a 2.9 mm thick $[PPh_4][FeCl_4]$ crystal: (a) z-polarized spectrum; (b) x,y-polarized spectrum. The solid vertical line indicates a grating change, which is responsible for the discontinuity.

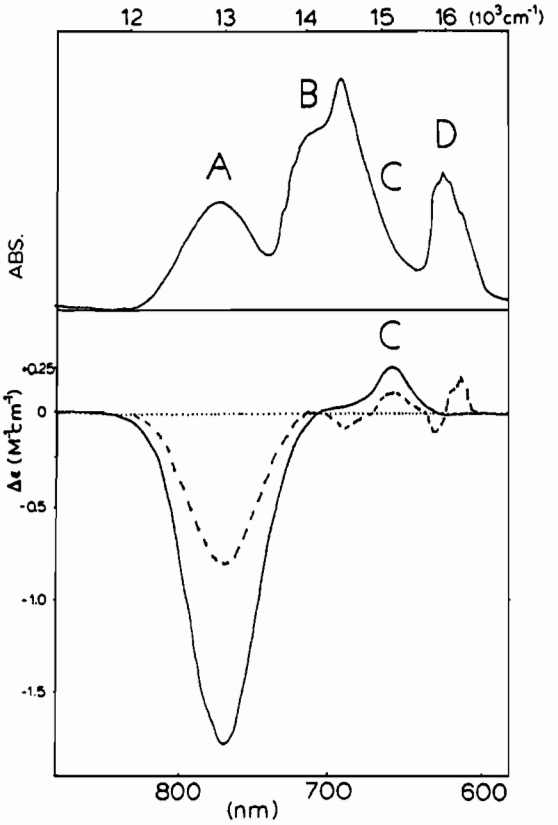

Figure 5. MCD spectra of $[PPh_4][FeCl_4]$ for region I. The x,y-polarized absorption spectrum is displayed on the same scale. The $\Delta\epsilon$ scale applies for the solid line, representing the 5 K and 50 kG MCD spectrum on a 0.5 mm thick crystal. The dashed line represents the 40 K and 50 kG spectrum.

D lose all their intensity while band A shows a 50% increase.

The MCD spectrum for region I at 5 T and 2 K is given in Figure 5. The zero magnetic field x,y-polarized absorption spectrum is also plotted in Figure 5 for comparison, since in the case of uniaxial crystals it is necessary, but not sufficient, for a band to have x,y-polarized intensity in order to have nonzero MCD intensity. In Figure 5, band A has a strong negative MCD signal. In the 2 K spectrum, bands B and D show no MCD as expected since they also have no linear x,y-polarized intensity under these conditions of high field and low temperature (Figure 4b). However, band C is now clearly observed as a positive MCD peak at 15 210 cm^{-1}. When the temperature is raised to 40 K (dashed curve in Figure 5), $M = -5/2$ is no longer the only ground-state Zeeman sublevel populated and weak MCD features appear corresponding to bands B and D.

Region II. The temperature dependence of the polarized absorption spectrum for region II is presented in Figure 6. In z polarization (Figure 6a), lowering the temperature to 4 K causes some sharpening of fine structure but no change in overall band shape or intensity. However, in x,y polarization (Figure 6b) there is an intensity increase that appears toward the high-energy side of band F.

In the TZE experiment with light polarized parallel to the z axis (Figure 7a), the intensity at 2 K exhibits a small decrease (~8%) at high field when integrated over both bands E and F. Likewise, in x,y polarization there is approximately a 6% decrease in the intensity at high field. It is apparent that some components of this band system show intensity increases while others show decreases in the TZE experiments. However, these various components overlap to such an extent that the changes in the intensity for each component are not resolved. Note that the intensities of several sharp but weak peaks at energies above band F also exhibit a dependence upon field.

Bands E and F are resolved clearly in the MCD spectrum at 5 T and 2 K (Figure 8), where band E exhibits a negative and band F a positive MCD signal.

Region III. The high-resolution polarized absorption spectrum of region III at 5 K is presented in Figure 9. Starting at low energy, there are three very sharp but weak peaks followed by the more intense band G, which is strongly x,y polarized. At higher energy (22 270 cm^{-1}) there is a weak feature (22 520 cm^{-1}), which may be part of band G. The spectra broaden considerably with increasing temperature (not shown), obscuring any temperature dependence of polarization ratios or low-symmetry splittings.

In the TZE with the magnetic field parallel to the S_4 axis, the intensity of band G approaches zero in z polarization (Figure 10a), while the intensity increases substantially for two of the weak, sharp peaks at lower energy. In x,y polarization with high field at low temperature (Figure 10b), band G increases by about 50% while the two lower energy features go to zero.

Band G also exhibits a negative MCD feature (Figure 11), while the weak, sharp features at lower energy have no MCD signal at 5 T and 2 K.

C. Charge-Transfer Transitions. The charge-transfer (CT) transitions of $FeCl_4^-$ may be observed up to 45 000 cm^{-1} in crystals with nonabsorbing counterions. The unpolarized spectrum of $[NBu_4][(Ga:Fe)Cl_4]$ (0.1% nominal Fe concentration) is shown in Figure 12. This is similar to the mull spectrum obtained by Bird and Day,[18] with somewhat better resolution. Unfortunately this salt is not crystallographically defined, but absorption spectra polarized along the extinction directions of the crystal (not shown) exhibit no significant polarization effects.

(18) Bird, B. D.; Day, P. *J. Chem. Phys.* **1968**, *49*, 392.

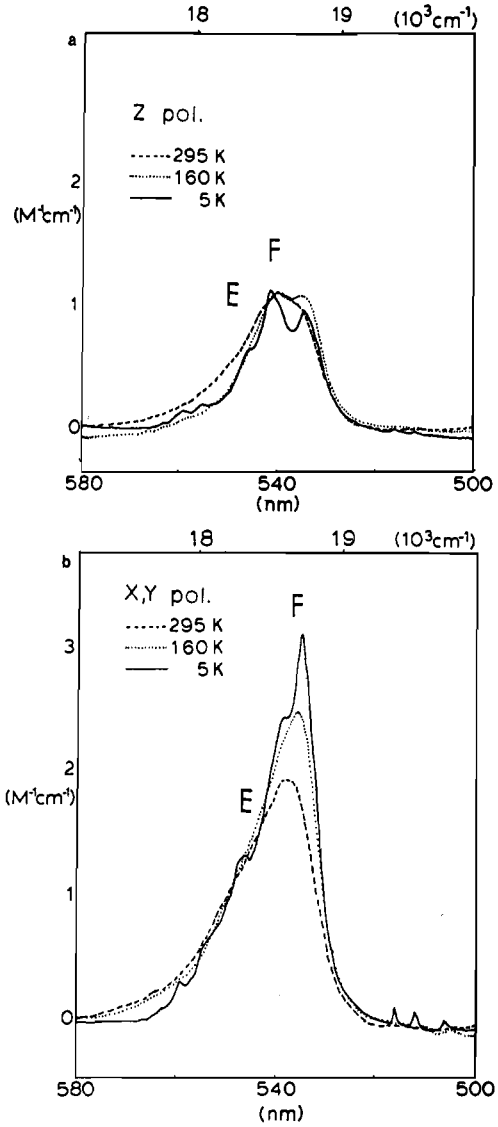

Figure 6. Polarized absorption spectra of region II for a 0.9 mm thick $[PPh_4][FeCl_4]$ crystal: (a) z-polarized spectrum; (b) x,y-polarized spectrum.

Only the lowest energy CT transition may be observed in the PPh_4^+ salt below the counterion absorbance (Figure 12, insert). This band exhibits an $x,y:z$ polarization ratio of 1.21 at room temperature, which increases to 1.27 upon cooling to 5 K. The deviation of the polarization ratio from unity for the fully allowed transition is due to the larger projection that the electric field vector makes upon the D_{2d} compressed $FeCl_4^-$ complex in x,y compared to that in z polarization. The square of the ratio of these projections calculated from the room-temperature crystal structure correctly predicts the observed polarization ratio at 295 K. From the low-temperature polarization ratio it is calculated that the Cl–Fe–Cl angle bisected by the distortion axis increases from the room-temperature value of 114.6° to about 115.6°.

Analysis

A. Group Theory. (i) Selection Rules. The LF transitions in high-spin d^5 ions are all spin-forbidden. In crystals composed of discrete, noninteracting complexes, these transitions gain intensity through spin–orbit coupling. Two possible spin–orbit mechanisms for intensity must be considered.[19] In the first mechanism, $^4T_1$ excited-state character is mixed into the $^6A_1$ ground state via the spin–orbit interaction. For this problem, tetragonal basis functions are most appropriate since the pure x,y polarization of the lowest energy band (Figure 2) indicates that the low-symmetry crystal

(19) Vala, M.; Rivoal, J. C.; Badoz, M. *Mol. Phys.* **1975**, *30*, 1325.

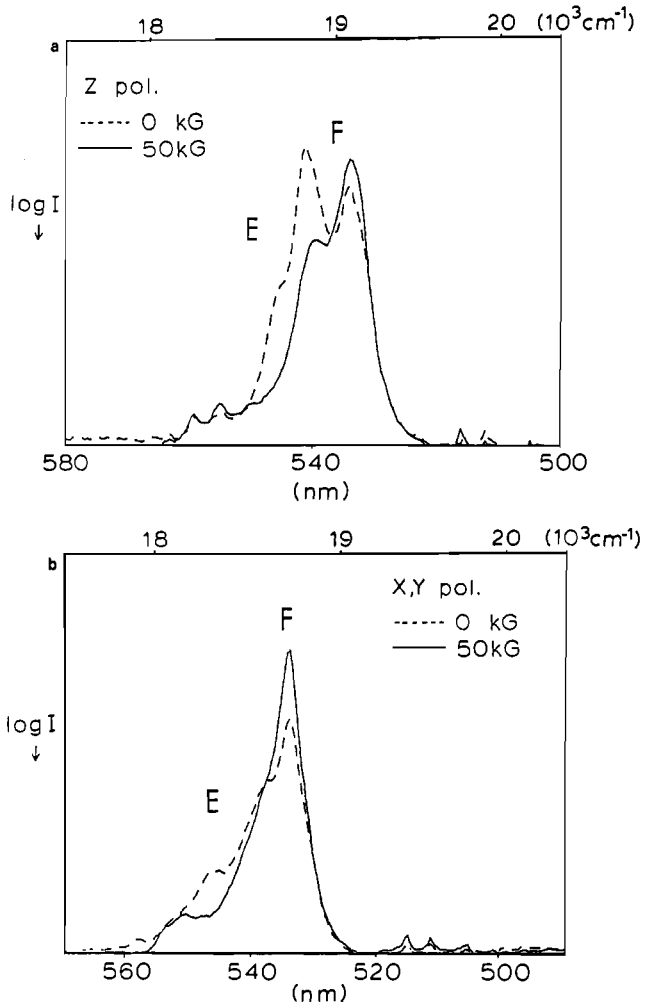

Figure 7. Transverse Zeeman effect for region II at 2 K with no field and a 50-kG magnetic field applied parallel to the S_4 axis of $[PPh_4][FeCl_4]$: (a) z-polarized spectrum for a 2.9 mm thick crystal. (b) x,y-polarized spectrum for a 0.8 mm thick crystal.

field is dominant over in-state spin–orbit splitting of the excited state. With use of a perturbation treatment in the $ShM\theta$ coupling scheme, the transition moment integral for the absorption process via the first mechanism may be expressed as

$$\langle {}^5/_2A_1M|m_n|{}^3/_2hM'\theta'\rangle = \langle {}^5/_2A_1M|H_{so}|{}^3/_2T_1M''\theta''\rangle \times \langle {}^3/_2T_1M''\theta''|m_n|{}^3/_2hM'\theta'\rangle / (E({}^6A_1) - E({}^4T_1)) \quad (2)$$

M is the S_z component of the total spin, S. h is an irreducible representation for the orbital part of the wave function, and θ is one of the degenerate partners of h. m_n is the electric dipole operator and transforms as the nth partner of the T_2 irreducible representation in T_d symmetry. In the real tetragonal system, n may be x, y, or z and in the complex tetragonal system -1, 0, or $+1$, where $m_{\pm 1} = m_x \pm im_y$ and $m_0 = -im_z$.

In the second possible spin–orbit mechanism, electric dipole allowed $^6T_2$ states mix into the ^4h LF excited states. The transition moment for this mechanism is given by eq 3.

$$\langle {}^5/_2A_1M|m_n|{}^3/_2hM'\theta'\rangle = \langle {}^3/_2hM'\theta'|H_{so}|{}^5/_2T_2M''\theta''\rangle \times \langle {}^5/_2T_2M''\theta''|m_n|{}^5/_2A_1M\rangle / (E({}^4h) - E({}^6T_2)) \quad (3)$$

The irreducible tensor method (Wigner–Eckart theorem) may be applied to factor the spin–orbit coupling matrix elements contained in eq 2 and 3 into products of reduced matrix elements and vector coupling coefficients according to eq 9.29 of Griffith:[9]

$$\langle ShM\theta|H_{so}|S'h'M'\theta'\rangle = \sum_i (-1)^{i+1+S-M}[-1]^{h+\theta} V\begin{bmatrix} S & S' & 1 \\ -M & M' & i \end{bmatrix} \times V\begin{bmatrix} h & h' & T_1 \\ -\theta & \theta' & -i \end{bmatrix} \langle Sh||\sum_k s\cdot\mu(k)||S'h'\rangle \quad (4)$$

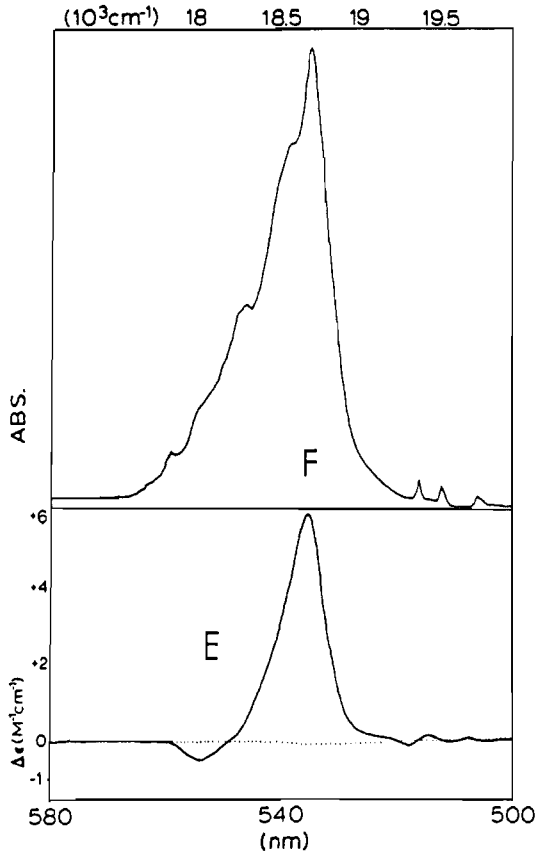

Figure 8. MCD spectrum of $[PPh_4][FeCl_4]$ for region II. The x,y-polarized absorption spectrum is displayed on the same scale. The spectrum was taken at 5 K and 50 kG on a 0.5 mm thick crystal.

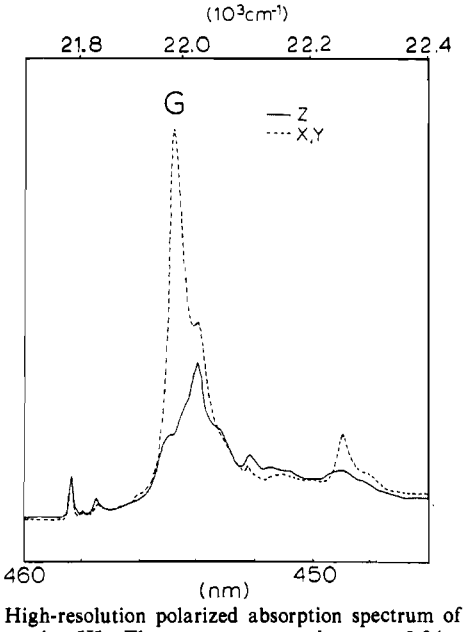

Figure 9. High-resolution polarized absorption spectrum of $[PPh_4][FeCl_4]$ for region III. The spectrum was taken on a 0.34 mm thick crystal.

$\langle Sh||\sum_k s\cdot\mu(k)||S'h'\rangle$ is the reduced matrix element for spin–orbit coupling with the operator written as a sum of the k one-electron operators. The reduced matrix element does not depend on the M and θ partners of the wave functions, and it is therefore not necessary to calculate the value of the reduced matrix element to obtain relative transition probabilities.

$$\bar{V}\begin{bmatrix} S & S' & 1 \\ -M & M' & i \end{bmatrix}$$

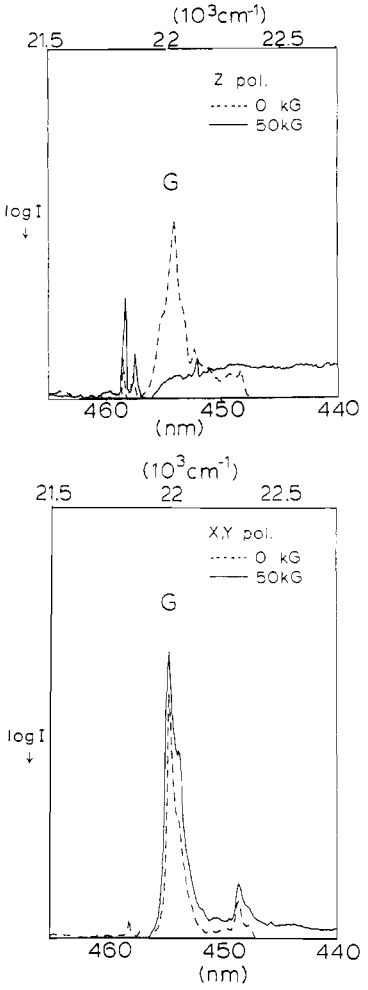

Figure 10. Transverse Zeeman effect for region III at 2 K with no field and a 50-kG magnetic field applied parallel to the S_4 axis of a 0.34 mm thick $[PPh_4][FeCl_4]$ crystal: (a) z-polarized spectrum; (b) x,y-polarized spectrum. Note that the base line shift is due to single-beam detection of the data.

is equivalent to a Wigner $3j$ symbol where the spin operator transforms as 1 with complex components i of -1, 0, and $+1$.

$$V\begin{bmatrix} h & h' & T_1 \\ -\theta & \theta' & -i \end{bmatrix}$$

is a Griffith V coefficient that describes the coupling of the orbital parts of the wave functions and the orbital angular momentum operator. The orbital operator transforms as T_1 and has complex components, $-i$, of -1, 0, and $+1$. The $\bar{V}$ values are found in the tables of Rotenberg et al.,[20] and the V coefficients are given by Griffith.[9] $(-1)^{i+1+S-M}[-1]^{h+\theta}$ is a phase factor where $[-1]^{h+\theta}$ is defined by Griffith. $[-1]^h = 1$ for h = T_2, E, A_1, or any component thereof, and $[-1]^h = -1$ for h = T_1, A_2, or any component thereof.

The matrix elements for the electronic dipole operator contained in the right-hand sides of eq 2 and 3 do not depend on spin and are given as

$$\langle ShM\theta|m_n|Sh'M'\theta'\rangle = \delta_{SS'MM'}[-1]^{T_2+n}V\begin{bmatrix} h & h' & T_1 \\ -\theta & \theta' & n \end{bmatrix}\langle Sh||m||S'h'\rangle \quad (5)$$

Note that evaluation of eq 2 by eq 4 and 5 involves a product of two V coefficients, $[V(A_1T_1T_1)][V(T_1T_2h)]$, while evaluation of eq 3 involves $[V(hT_1T_2)][V(A_1T_2T_2)]$. These products are the same within a phase factor and produce identical selection rules for the two intensity mechanisms expressed by eq 2 and 3. Also

(20) Rotenberg, M.; Bivins, R.; Metroplis, N.; Wooten, J. K. *The 3j and 6j Symbols*; Technology Press: Boston, 1959.

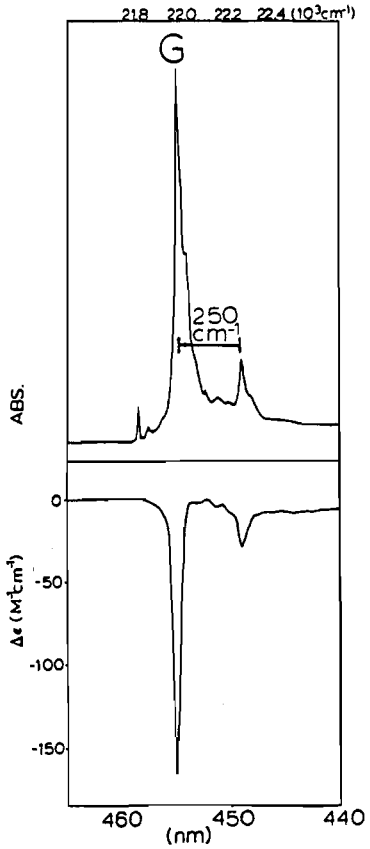

Figure 11. MCD spectrum of $[PPh_4][FeCl_4]$ for region III. The x,y-polarized absorption spectrum is displayed on the same scale. The spectrum was taken at 5 K and 50 kG MCD on a 0.5 mm thick crystal.

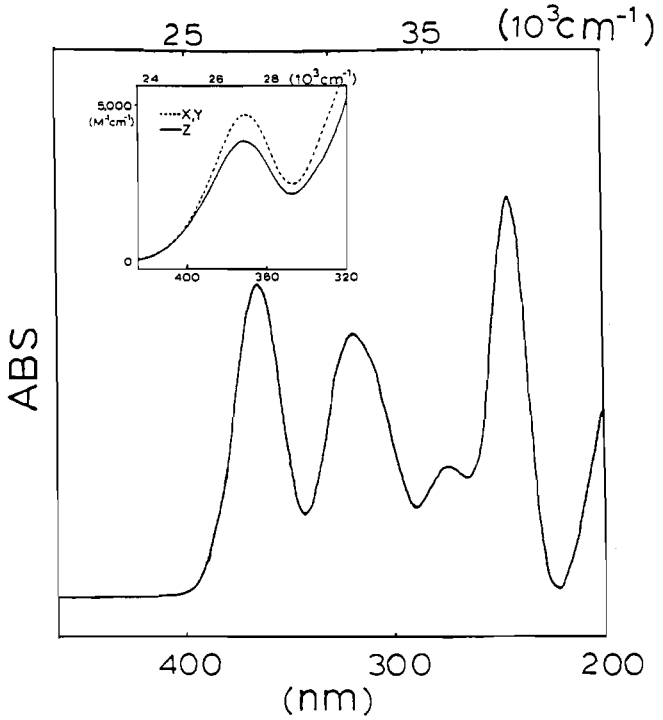

Figure 12. Unpolarized absorption spectrum of 0.1% $[NBu_4][(Ga:Fe)Cl_4]$ at 6 K. The inset is the polarized absorption spectrum of 0.5% $[PPh_4][(Ga:Fe)Cl_4]$ at 295 K.

note that $^4A_1$ is predicted to have no intensity in T_d since all $V(A_1T_2T_1)$ values are zero.

The calculations for eq 2 and 3 have been carried out by earlier workers, and certain of the results have been published.[19,21] However, it has been necessary to prepare a complete tabulation of the transition moments in order to derive selection rules for the experiments presented here. In particular, the low-temperature, high magnetic field experiments require comparison of the matrix elements involving the $M = -^5/_2$ ground-state sublevel to the average of the matrix elements for all ground-state M levels. Furthermore, the matrix elements for the tetragonal basis functions are required rather than the spinor basis functions since the strong polarization of the spectrum (Figure 2) implies that the D_{2d} splitting of the T_d parent wave functions is greater than the SO interactions. The transition moments for each polarization m_n in the complex tetragonal system calculated by eq 2 and 3 between each $|^5/_2A_1M\rangle$ partner of the 6-fold degenerate ground state and each $|ShM\theta\rangle$ partner of the $^4T_1$, $^1T_2$, ^4E, and $^4A_2$ excited states are given in Table II in terms of reduced matrix elements.

The relative intensities for absorption of plane-polarized light are calculated by using eq 6. λ is the ground-state degeneracy,

$$I_z = (1/N\lambda)\sum_{MM'}|\langle{}^5/_2A_1M|m_0|{}^3/_2hM'\theta'\rangle|^2 \quad (6a)$$

$$I_x = I_y = (1/2N\lambda)\sum_{MM'}\{|\langle{}^5/_2A_1M|m_{+1}|{}^3/_2hM'\theta'\rangle|^2 + |\langle{}^5/_2A_1M|m_{-1}|{}^3/_2hM'\theta'\rangle|^2\} \quad (6b)$$

which is equal to 6. N is a factor chosen in terms of the reduced matrix elements such that the relative intensities I_z and $I_{x,y}$ come out as simple whole numbers. I_z and $I_{x,y}$ are given in Table III for each orbital partner, θ, of each ^4h state in the real tetragonal system.

Also found in Table III are the selection rules for the low-temperature TZE experiments, $I_z(-^5/_2)$ and $I_{x,y}(-^5/_2)$, which are the ratios of the polarized intensity under conditions where only the $M = -^5/_2$ level of the ground state is populated to the intensity under conditions where all ground-state levels are equally populated. These ratios are calculated as

$$I_z(-^5/_2) = (1/N)\sum_{M'}|\langle{}^5/_2\ A_1\ -^5/_2|m_0|{}^3/_2hM'\theta'\rangle|^2/I_z \quad (7a)$$

$$I_{x,y}(-^5/_2) = (1/2N)\sum_{M'}\{|\langle{}^5/_2\ A_1\ -^5/_2|m_{+1}|{}^3/_2hM'\theta'\rangle|^2 + |\langle{}^5/_2\ A_1\ -^5/_2|m_{-1}|{}^3/_2hM'\theta'\rangle|^2\}/I_{x,y} \quad (7b)$$

All bands in the MCD spectrum were observed to be temperature dependent, and therefore only C terms need be considered.[22] In the limit of Curie law behavior, the C_0/D_0 terms are calculated as[22]

$$C_0/D_0 = [(1/\lambda)\sum_{MM'}gM\{|\langle{}^5/_2A_1M|m_{+1}|{}^3/_2hM'\theta'\rangle|^2 - |\langle{}^5/_2A_1M|m_{-1}|{}^3/_2hM'\theta'\rangle|^2\}]/NI_{x,y} \quad (8)$$

The denominator, $NI_{x,y}$, is the dipole strength (D_0) in x,y polarization. The C_0/D_0 terms are also given in Table III. The last column in Table III, $(C_0/D_0)_{tot}$, is the value of the C_0/D_0 term in the case where the splitting of the orbital partners, θ, of a given ^4h by the tetragonal crystal field are not resolved and is identical with the values calculated by Rivoal et al.[21] Note that under conditions of total saturation where only the $M = -^5/_2$ level is populated, the absolute values of the nonzero C_0/D_0 terms approach unity, but the signs are the same as for the nonsaturating (Curie law) conditions given in Table III.

(ii) Band Assignments. Region I. Band A is completely x,y polarized (Figure 3), which is a selection rule for the z orbital partner of a $^4T_1$ or $^4T_2$ state (Table III, $I_{x,y}$ and I_z). The 50% intensity increase observed in the TZE (Figure 4b) is also the behavior predicted for the z orbital partner of a $^4T_1$ or $^4T_2$ state (Table III, $I_{x,y}(-^5/_2)$). Finally, the negative sign observed in the MCD for band A (Figure 5) distinguishes the band as $^4T_1{}^az$ (Table III, C_0/D_0).

Band B exhibits mixed polarization (Figure 3). However, the x,y intensity drops to zero in the TZE while the z intensity increases by 50% (Figure 4). This behavior is characteristic of the x,y partners of either $^4T_1$ or $^4T_2$ states (Table III, $I_{x,y}(-^5/_2)$ and

(21) Rivoal, J. C.; Briat, B.; Vala, M. *Mol. Phys.* **1983**, *38*, 1829.

(22) Stephens, P. J. *Adv. Chem. Phys.* **1976**, *35*, 197.

Table II. Transition Moments $\langle {}^5/_2A_1M|m_n|{}^3/_2hM'\theta'\rangle$ for the High-Spin d^5 Ligand Field Spin-Forbidden Transitions in T_d Symmetry (Complex Tetragonal Basis) Expressed in Units of $R \pm S$ Where

$$R = (\langle {}^5/_2T_2||H_{so}||{}^3/_2h\rangle\langle T_2||m||A_1\rangle)(E({}^4h) - E({}^6T_2)) \qquad S = (\langle {}^3/_2T_1||H_{so}||{}^5/_2A_1\rangle\langle h||m||T_1\rangle)/(E({}^6A_1) - E({}^4T_1))$$

(a) Transition Moments for $|{}^5/_2A_1M\rangle \rightarrow |{}^3/_2T_1M'\theta'\rangle$ in Units of $R + S$

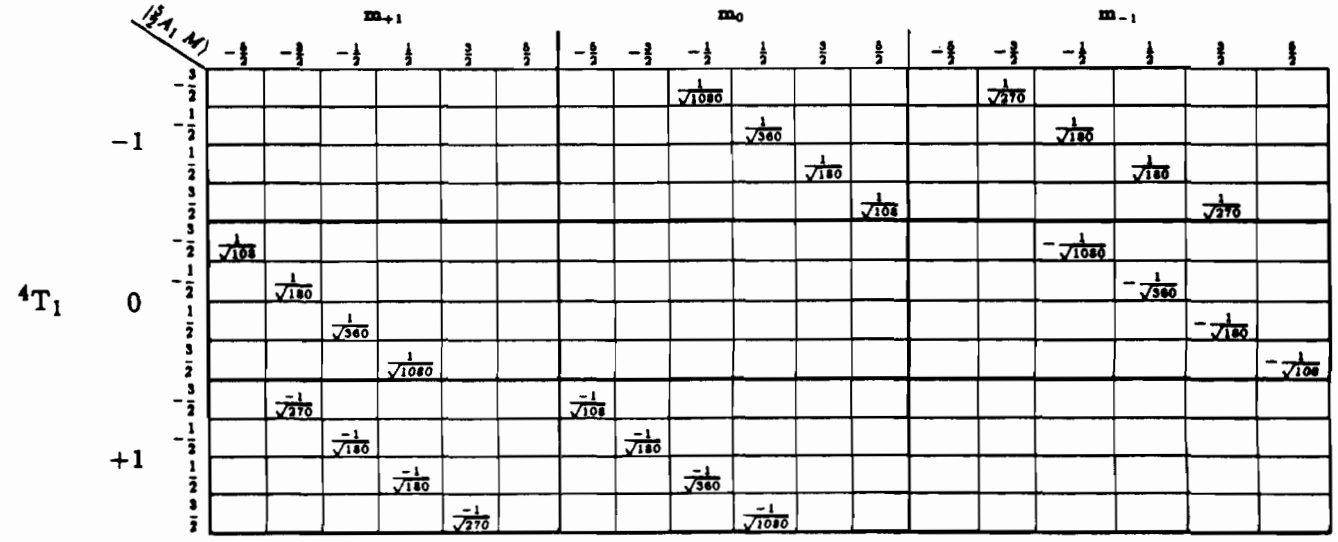

(b) Transition Moments for $|{}^5/_2A_1M\rangle \rightarrow |{}^3/_2T_2M'\theta'\rangle$ in Units of $R - S$

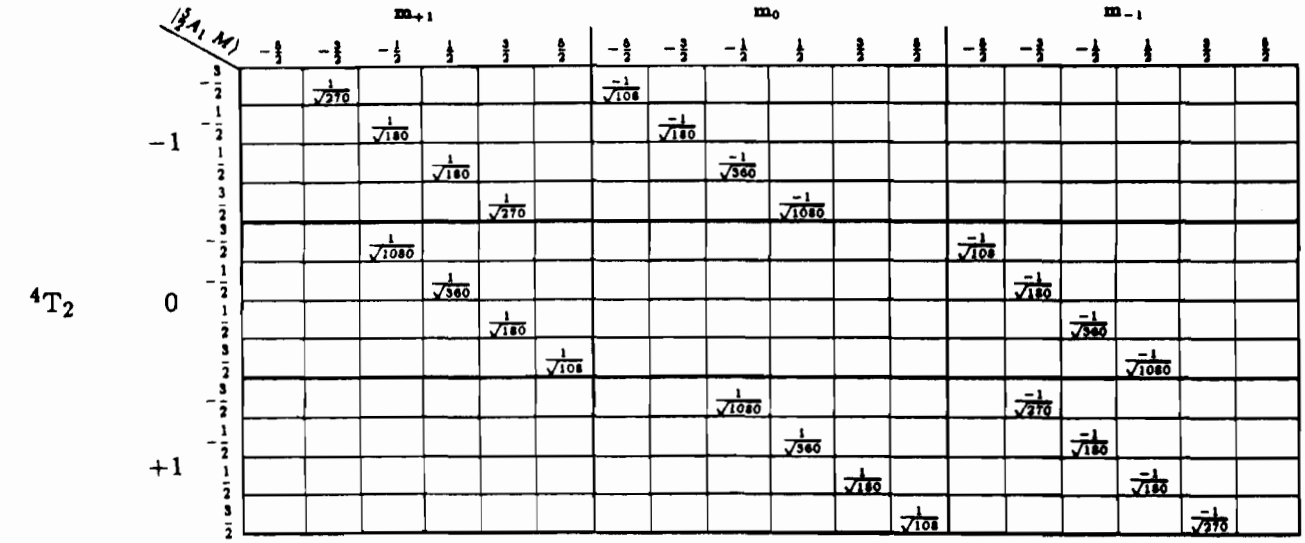

(c) Transition Moments for $|{}^5/_2A_1M\rangle \rightarrow |{}^3/_2EM'\theta'\rangle$ in Units of $R - S^a$

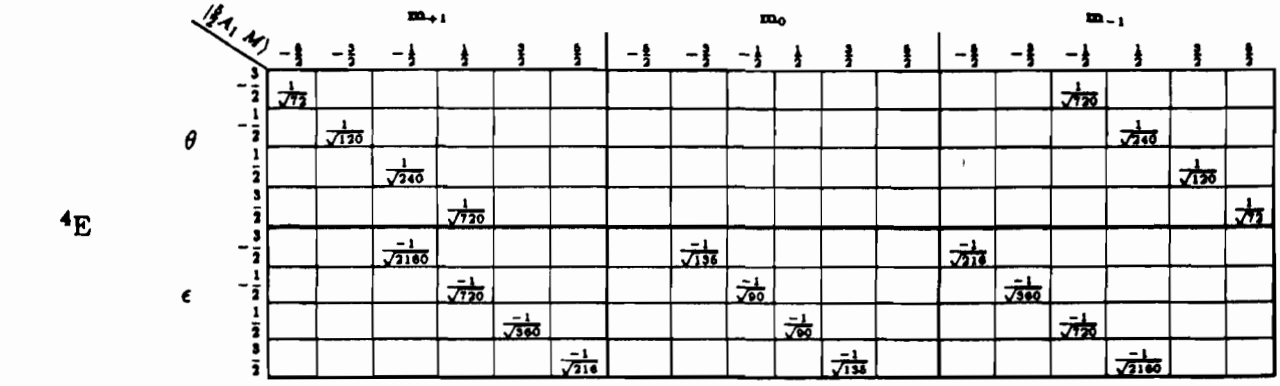

(d) Transition Moments for $|{}^5/_2A_1M\rangle \rightarrow |{}^3/_2A_2M'\rangle$ in Units of $R - S^b$

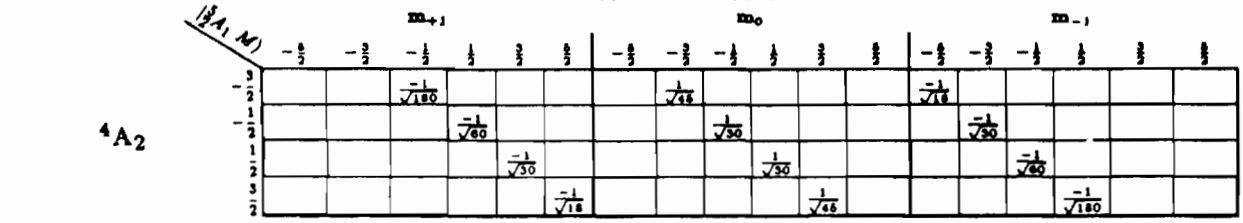

[a] The use of θ as a general symbol for an orbital of an irreducible representation of h should not be confused with its use as specific orbital partner of an E state. [b] The $^4A_2$ transition is not observed in this work, but this table has been included for completeness.

Table III. Selection Rules for Polarized Absorption, Transverse Zeeman Effect, and Magnetic Circular Dichroism of the Spin-Forbidden d^5 LF Transitions

^4h	θ	I_z	$I_{x,y}$	$I_z(-5/2)$	$I_{x,y}(-5/2)$	C_0/D_0	$(C_0/D_0)_{tot}$
$^4T_1$	z	0	1	...	1.5	−7	$-7/2$
	x,y	2	1	1.5	0	0	
$^4T_2$	z	0	1	...	1.5	+7	$+7/2$
	x,y	2	1	1.5	0	0	
^4E	θ	0	3	...	1.5	−7	$-7/2$
	ϵ	4	1	0	1.5	+7	
$^4A_1$	...	...	...	...	...	...	...
$^4A_2$	...	1	1	0	1.5	+7	+7

$I_z(-5/2)$). Band B is thus assigned as $^4T_1{}^a x,y$ since the z orbital component of the low-symmetry-split $^4T_1{}^a$ is found immediately to lower energy as band A. The MCD of band B is zero at 2 K and 5 T (Figure 5), also in agreement with the $^4T_1{}^a x,y$ assignment (Table III, C_0/D_0). However, at higher temperature, some weak MCD features appear (dashed curve in Figure 5). In the absence of in-state SO coupling in $^4T_1 x,y$, the C term is predicted to be zero at the higher temperature because each ground-state M sublevel absorbs left and right circularly polarized light equally. Therefore, the appearance of the weak MCD features at higher temperatures indicates that there must be a further fine-structure splitting (due to in-state SO coupling, which produces a pseudo-A term arising from oppositely signed C terms). Since the z-polarized intensity in the TZE (Figure 4a) increases uniformly across the entire band, the double-hump appearance of this band is probably due to vibronic band-shape effects.

Band C is not clearly observed in the polarized absorption or TZE since it is weak and is obscured by other bands. However, it is clearly observed in the MCD at 2 K (Figure 5), and the positive sign of the MCD signal leads to an assignment as $^4T_2{}^a z$. The x,y intensity of band D drops to zero in the TZE while the z intensity increases by ~50% (Figure 4), leading to its assignment as $^4T_2{}^a x,y$. This band has zero MCD under saturating conditions, but again at higher temperature a weak pseudo-A MCD feature appears. The z intensity in the TZE increases (Figure 4a) more for some components of this band than others. A nonuniform response of the fine-structure intensities to magnetic field is also observed in the TZE with the field perpendicular to the low-symmetry crystal field (not shown). It is concluded that for the $^4T_2{}^a x,y$ the fine structure is due to in-state SO coupling, which should not be quenched by the axial distortion.

Region II. The TZE (Figure 7) suggests that this region consists of two overlapping transitions (bands E and F) since the observed $I_z(-5/2) = 0.92$ and $I_{x,y}(-5/2) = 0.94$ are not characteristic of any one transition. The MCD under saturating conditions (Figure 8) confirms this by resolving two peaks, one of negative sign (band E) and one of positive sign (band F). On the basis of the MCD signs, band E is assigned as $^4E^a$ while band F is assigned as $^4T_2{}^b$. Note that the $^4E^a$ and $^4T_2{}^b$ states should not be strongly split by the low-symmetry distortion (relative to $^4T_1{}^a$ and $^4T_2{}^a$) as they mostly derive from the $t_2{}^3e^2$ configuration.

There are also three very weak transitions above $^4T_2{}^b$ around 19 500 cm^{-1}. These appear to be too far separated in energy from the $^4E^a$ and $^4T_2{}^b$ to be reasonably assigned as fine-structure or vibrational progressions of those transitions. Furthermore, they do not exhibit selection rules of any of the quartet states in the TZE and MCD experiments. The fact that their intensities change in the TZE experiments (Figure 7) demonstrates that they are spin-forbidden. It is likely that these are highly forbidden transitions to doublet states. Considering the sharpness of the peaks, they must by ligand field independent states, but specific assignments are not considered here.

Region III. Band G loses all z-polarized intensity in the TZE experiment (Figure 10a), which is a selection rule for a ^4E state (Table III, $I_z(-5/2)$). The 50% increase in x,y polarization (Figure 10b) is also the behavior predicted for ^4E (Table III, $I_{x,y}(-5/2)$). The negative MCD (Figure 11) confirms the assignment as $^4E^b$. Most of the weak features to higher energy are assigned as weakly coupled vibrational progressions. However, the very sharp, weak features to lower energy of $^4E^b$ exhibit behavior in TZE and MCD that could not be associated with any of the ligand field quartets and are therefore assigned as doublets.

Table IV. Observed Magnetooptical Characteristics and Assignments of the LF Transitions in $[PPh_4][FeCl_4]$

band	$I_z(-5/2)$	$I_{x,y}(-5/2)$	MCD	assignt	energy, cm^{-1} obsd	energy, cm^{-1} obsd	energy, cm^{-1} calcd[a]
A[b]	...	1.66	−	$^4T_1{}^a z$	12 890	13 790[c]	13 554
B	1.50	0	0	$^4T_1{}^a x,y$	14 240		
C[d]	...	...	+	$^4T_2{}^a z$	15 210	15 770[c]	15 880
D	1.69	0	0	$^4T_2{}^a x,y$	16 050		
E[e]	...	...	−	$^4E^a$	18 200		18 076
F[e]	...	...	+	$^4T_2{}^b$	18 800		19 896
G	0	1.45	−	$^4E^b$	22 008		21 181

[a] Energies calculated by a fit of observed energies to the Tanabe–Sugano matrices. Dq = 655 cm^{-1}; B = 444 cm^{-1}; C = 2728 cm^{-1}. [b] Band A is purely x,y polarized. [c] Indicates barycenter of low-symmetry-split band. [d] TZE for band C is not clearly observed due to overlap with more intense bands; resolved and assigned by MCD at 2 K and 5 T. [e] Bands E and F are not resolved in TZE.

The results of the magnetooptical experiments and the complete set of band assignments for the ligand field transitions in Figure 2 are summarized in Table IV.

A general observation concerning the polarization ratios of all the bands should be emphasized. The polarized absorption spectrum in Figure 2 shows that the z-polarized intensity summed over all orbital components of a given transition is not equal to the total x,y-polarized intensity of the same transition. However, Table III predicts these to be equal. In the derivation of these selection rules, the use of a SO coupling reduced matrix element (eq 4) common to all orbital partners of a given state in cubic symmetry was used. This assumes that the D_{2d} distortion produces only an energy splitting of the orbital components with no change in the cubic wave functions. However, the observed polarization ratios require that reduced matrix elements appropriate for D_{2d} symmetry be considered. For the intensity mechanism via $^4T_1$ SO coupling to the ground state, the D_{2d} reduced matrix elements originating from $^4T_1 z$ and $^4T_1 x,y$ orbital partners are not necessarily equal:

$$\langle {}^5/_2A_1 || H_{so} || {}^3/_2T_1 z \rangle \neq \langle {}^5/_2A_1 || H_{so} || {}^3/_2T_1 x,y \rangle \qquad (9)$$

The reason for this inequality is that, in the process of lifting the degeneracy of the cubic wave functions, the tetragonal (D_{2d}) distortion can create some anisotropies in covalent interactions of the one-electron orbitals. In the next section this idea will be expanded in detail, as it is also necessary for an understanding of the origin of the ground-state ZFS.

B. Origin of Zero-Field Splitting. There are two mechanisms that contribute to ZFS of the $^6A_1$ ground state of axially distorted high-spin d^5 transition-metal ions. These are spin–spin coupling within the ground state and second-order spin–orbit coupling to low-symmetry-split excited states. The spin–spin contribution has been estimated to be on the order of 10^{-3} cm^{-1} and to be positive.[23]

(23) (a) Watanabe, H.; Kishishita, H. *Prog. Theor. Phys.* **1970**, *46*, 1. (b) Watanabe, H. *J. Phys. Chem. Solids* **1964**, *25*, 1471. (c) Watanabe, H. *Prog. Theor. Phys.* **1957**, *18*, 405.

Typical ZFS splittings in Fe(III) complexes are much larger, and thus the spin–spin contribution is usually neglected. This leaves the spin–orbit mechanism as the dominant contribution to D. Griffith[5] developed a model to explain the ZFS observed in axially distorted high-spin d^5 systems in terms of second-order spin–orbit coupling of the ground state to excited LF states. In cubic symmetry the ground state can only spin–orbit couple to the three LF $^4T_1$ states (a, b, c). In the Griffith model a ZFS arises when an axial distortion causes a splitting of the excited LF $^4T_1$ states, which in turn affects the energy denominators in the second-order energy correction to the ground-state M spin states. When this second-order energy correction to each M spin state in the $^6A_1$ ground state is summed over all M components, the following equation for D arising from any $^4T_1$ is obtained

$$D(^4T_1) = [|\langle {}^3/_2T_1z||H_{so}||{}^5/_2A_1\rangle|^2/E_z - |\langle {}^3/_2T_1x,y||H_{so}||{}^5/_2A_1\rangle|^2/E_{x,y}]/180 \quad (10)$$

where E_z and $E_{x,y}$ are the energies of the z and x,y components of the low-symmetry-split $^4T_1$. $\langle {}^3/_2T_1z||H_{so}||{}^5/_2A_1\rangle$ and $\langle {}^3/_2T_1x,y||H_{so}||{}^5/_2A_1\rangle$ are the spin–orbit coupling reduced matrix elements in axial symmetry indexed according to their cubic parent. In order to evaluate eq 10, expressions for the matrix elements are required. Griffith assumed that spin–orbit coupling matrix elements between the $^4T_1$ low-symmetry components and $^6A_1$ can be evaluated using cubic wave functions and pure d orbitals. This leads to $\langle {}^3/_2T_1z||H_{so}||{}^5/_2A_1\rangle = \langle {}^3/_2T_1x,y||H_{so}||{}^5/_2A_1\rangle = 6\zeta_{Fe^{3+}}$, for spin–orbit coupling between the first or third pure strong-field $^4T_1$ states ($t_2^2e^3$(a), $t_2^4e^1$(c)) and the ground state, while $\langle {}^3/_2T_1z||H_{so}||{}^5/_2A_1\rangle = \langle {}^3/_2T_1x,y||H_{so}||{}^5/_2A_1\rangle = 18^{1/2}\zeta_{Fe^{3+}}$ for spin–orbit coupling between the second pure strong-field $^4T_1$ state ($t_2^3e^2$(b)) and the ground state. $\zeta_{Fe^{3+}}$ is the Fe^{3+} free ion spin–orbit coupling constant (430 cm^{-1}). The Griffith model then gives the following contributions to D:

$$D(^4T_1{}^{a,c}) = \zeta_{Fe^{3+}}{}^2(1/E_z - 1/E_{x,y})/5 \quad (11a)$$

$$D(^4T_1{}^{b}) = \zeta_{Fe^{3+}}{}^2(1/E_z - 1/E_{x,y})/10 \quad (11b)$$

The total D is just the sum of the contributions from the individual $^4T_1$ states. To date these expressions have not been tested experimentally because the low-symmetry components of the $^4T_1$ states have not been assigned in any ferric complexes. From the observed energies of 12920 cm^{-1} ($^4T_1{}^a z$) and 14240 cm^{-1} ($^4T_1{}^a x,y$) at 6 K and a spin–orbit coupling constant of 430 cm^{-1}, $D(^4T_1{}^a)_{calc}$ = 0.27 cm^{-1}. To a first approximation the low-symmetry splitting of $^4T_1{}^b$ and its contribution to D is zero, because it derives mostly from the $t_2^3e^2$ strong-field configuration. $^4T_1{}^c$ should have a low-symmetry splitting that is of equal magnitude and opposite sign to the $^4T_1{}^a$ splitting, since it derives mostly from the $t_2^4e^1$ strong-field configuration. From a ligand field analysis (vide infra) of the observed spectrum the energies of the components of the low-symmetry-split $^4T_1{}^c$ are estimated to be 30650 cm^{-1} ($^4T_1{}^c z$) and 29300 cm^{-1} ($^4T_1{}^c x,y$). From eq 11a and these energies $D(^4T_1{}^c)$ = −0.05 cm^{-1}. Thus the total D calculated from Griffith's model is +0.22 cm^{-1}, which is opposite in sign to the experimental value of −0.042 cm^{-1}. This indicates that an additional effect must be active in producing the observed D.

We believe this effect must arise from covalency, which is neglected in the Griffith treatment. The effect of covalency on the spin–orbit interactions can be included in eq 10 by multiplying both matrix elements by a Stevens orbital reduction factor[24] (κ). This will reduce the magnitude of D_{calc} but cannot explain the sign change as κ^2 is a positive number less than 1. This assumes an isotropic κ; however, this is not appropriate in axial symmetry as spin–orbit coupling matrix elements between the different low-symmetry components of $^4T_1$ and the ground state ($\langle {}^3/_2T_1z||H_{so}||{}^5/_2A_1\rangle$, and $\langle {}^3/_2T_1x,y||H_{so}||{}^5/_2A_1\rangle$) are no longer required to be equal. In fact these matrix elements are clearly seen to be inequivalent on the basis of the observed polarization ratios of the ligand field transitions (vide supra, eq 9). When the matrix elements in eq 10 are replaced with the anisotropic expressions $\kappa_z\langle {}^3/_2T_1z||H_{so}||{}^5/_2A_1\rangle$ and $\kappa_{x,y}\langle {}^3/_2T_1x,y||H_{so}||{}^5/_2A_1\rangle$ the following expression is obtained:

$$D(^4T_1{}^{a,c}) = \zeta_{Fe^{3+}}{}^2[\kappa_z{}^2/E_z - \kappa_{x,y}{}^2/E_{x,y}]/5 \quad (12)$$

Since $E_{x,y} > E_z$ for $^4T_1{}^a$, the experimental sign of D requires that $\kappa_z{}^2 < \kappa_{x,y}{}^2$.

These orbital reduction factors can be related to covalency parameters in the complex by deriving expressions for the reduced matrix elements in eq 9 in terms of mixing coefficients between ligand LCAO's and Fe d orbitals. It is assumed that the t_2 metal set has only σ antibonding interactions, while the e metal set has only π antibonding interactions. It is also assumed that the ligand characters in the d_{z^2} and $d_{x^2-y^2}$ orbitals are equal, since these orbitals are only weakly antibonding. α is the amount of ligand character mixed into the d_{z^2} and $d_{x^2-y^2}$ orbitals, β the ligand character in the d_{xy} orbital, and γ the ligand character mixed into the $d_{xz,yz}$ orbitals. Table V gives the one-electron covalent wave functions used. For example, in Table V, p_{x1} represents a P_x orbital centered on ligand 1. The wave functions given are consistent with the Butler[25] phase convention. The coordinate system, T_d ligand LCAO's, and transformation matrices that take ligand-centered angular momentum into metal-centered angular momentum are described in Piepho and Schatz[26] (pp 294, 568–569). Using the irreducible tensor method, it is possible to express the spin–orbit coupling reduced matrix elements between multielectron wave functions in terms of reduced matrix elements between the one-electron wave functions given in Table V. These matrix elements can then be expressed as functions of α, β, γ, $\zeta_{Fe^{3+}}$, and ζ_{Cl^-} (the ligand spin–orbit coupling constant of 580 cm^{-1}). The evaluated matrix elements can then be used in eq 10.

By the above procedure the following expressions for spin–orbit coupling between the low-symmetry components of the two

Table V. One-Electron Wave Functions for D_{2d} $FeCl_4^-$

t_2 σ Metal Antibonding Set
$|xz\rangle^* = (1-\gamma^2)^{1/2}d_{xz} - \gamma\phi_1$
$|yz\rangle^* = -i(1-\gamma^2)^{1/2}d_{yz} - \gamma\phi_2$
$|xy\rangle^* = i(1-\beta^2)^{1/2}d_{xy} - \beta\phi_3$

e π Metal Antibonding Set
$|z^2\rangle^* = (1-\alpha^2)^{1/2}d_{z^2} - \alpha\phi_4$
$|x^2-y^2\rangle^* = (1-\alpha^2)^{1/2}d_{x^2-y^2} - \alpha\phi_5$

t_2 σ Ligand Bonding Set
$|xz\rangle = \gamma d_{xz} + (1-\gamma^2)^{1/2}\phi_1$
$|yz\rangle = \gamma d_{yz} + (1-\gamma^2)^{1/2}\phi_2$
$|xy\rangle = \beta d_{xy} + (1-\beta^2)^{1/2}\phi_3$

t_2 σ Ligand LCAO Set
$\phi_1 = (-i/2)[P_{x1} + P_{z2} - P_{z3} - P_{z4}]$
$\phi_2 = (-1/2)[P_{z1} - P_{z2} + P_{z3} - P_{z4}]$
$\phi_3 = (1/2)[P_{z1} - P_{z2} - P_{z3} + P_{z4}]$

e π Ligand LCAO Set
$\phi_4 = (-1/2)[P_{x1} - P_{x2} - P_{x3} + P_{x4}]$
$\phi_5 = (1/2)[P_{y1} - P_{y2} - P_{y3} + P_{y4}]$

e π Ligand Bonding Set
$|z^2\rangle = \alpha d_{z^2} + (1-\alpha^2)^{1/2}\phi_4$
$|x^2-y^2\rangle = \alpha d_{x^2-y^2} + (1-\alpha^2)^{1/2}\phi_5$

t_2 π Ligand LCAO Set (Nonbonding)
$|t_2\xi\rangle = (-1/4)[P_{x1} + P_{x2} - P_{x3} - P_{x4} + 3^{1/2}[-P_{y1} - P_{y2} + P_{y3} + P_{y4})]$
$|t_2\eta\rangle = (-i/4)[P_{x1} - P_{x2} + P_{x3} - P_{x4} + 3^{1/2}(P_{y1} - P_{y2} + P_{y3} - P_{y4})]$
$|t_2\zeta\rangle = (-1/2)[P_{x1} + P_{x2} + P_{x3} + P_{x4}]$

t_1 Ligand LCAO Set (Nonbonding)
$|t_1x\rangle = (-1/4)[3^{1/2}(-P_{x1} - P_{x2} + P_{x3} + P_{x4}) - P_{y1} - P_{y2} + P_{y3} + P_{y4}]$
$|t_1y\rangle = (i/4)[3^{1/2}(P_{x1} - P_{x2} + P_{x3} - P_{x4}) - P_{y1} + P_{y2} - P_{y3} + P_{y4}]$
$|t_1z\rangle = (1/2)[P_{y1} + P_{y2} + P_{y3} + P_{y4}]$

(24) Stevens, K. W. H. *Proc. R. Soc. London* **1953**, *A219*, 542.

(25) Butler, P. H. *Point Group Symmetry Applications: Methods and Tables*; Plenum Press: New York, 1981.

(26) Piepho, S. B.; Schatz, P. N. *Group Theory In Spectroscopy*; Wiley-Interscience: New York, 1983.

strong-field $^4T_1$ ($t_2^2e^3$, $t_2^4e^1$) states and the $^6A_1$ ground state are derived:

$$\langle {}^3/_2T_1{}^a z||H_{so}||{}^5/_2A_1\rangle = \langle {}^3/_2T_1{}^c a||H_{so}||{}^5/_2A_1\rangle = 6(1-\alpha^2)^{1/2}(1-\beta^2)^{1/2}\zeta_{Fe^{3+}} + i6^{1/2}\alpha\beta\zeta_{Cl^-} \quad (13a)$$

$$\langle {}^3/_2T_1{}^a x,y||H_{so}||{}^5/_2A_1\rangle = \langle {}^3/_2T_1{}^c x,y||H_{so}||{}^5/_2A_1\rangle = 6(1-\alpha^2)^{1/2}(1-\gamma^2)^{1/2}\zeta_{Fe^{3+}} + i6^{1/2}\alpha\gamma\zeta_{Cl^-} \quad (13b)$$

The matrix elements are indexed according to their tetrahedral parent; however, they represent the lower symmetry (D_{2d}) point group. In the limit of no covalency (i.e. $\alpha = \beta = \gamma = 0$) eq 12 reduces to $6\zeta_{Fe^{3+}}$. From eq 13 the following expressions for the orbital reduction factors of eq 12 are derived:

$$\kappa_z = (1-\alpha^2)^{1/2}(1-\beta^2)^{1/2} + i6^{-1/2}\alpha\beta\zeta_{Cl^-}/\zeta_{Fe^{3+}} \quad (14a)$$

$$\kappa_{x,y} = (1-\alpha^2)^{1/2}(1-\gamma^2)^{1/2} + i6^{-1/2}\alpha\gamma\zeta_{Cl^-}/\zeta_{Fe^{3+}} \quad (14b)$$

From Xα–SW calculations on the T_d $FeCl_4^-$ site[27] the covalency parameters are estimated to be $\alpha^2 = 0.16$ and $\beta^2 = \gamma^2 = 0.28$. In strict T_d symmetry it is required that $\gamma^2 = \beta^2$; however, in D_{2d} symmetry this restriction is removed. This anisotropy in covalency appears to be the physical origin of the empirical observation that $\kappa_z \neq \kappa_{x,y}$ in D_{2d} $FeCl_4^-$. When α^2 and $(\beta^2 + \gamma^2)/2$ are fixed at the Xα T_d values and the anisotropy $\beta^2 - \gamma^2$ is varied, a dramatic effect is calculated for D. If $\beta^2 > \gamma^2$, the contribution from $^4T_1{}^a$ becomes quenched, while the $^4T_1{}^c$ contribution is enhanced, making it more negative. The overall effect causes a reversal in the sign of D_{calc} from the Griffith model (eq 11). Varying $\beta^2 - \gamma^2$ to get agreement with D_{exp}, we find that $\beta^2 - \gamma^2 = 0.055$ gives $D = -0.04$ cm^{-1}. The fact that $\beta^2 > \gamma^2$ is required to obtain D_{exp} indicates that the d_{xy} antibonding orbital must be more covalent than the $d_{xz,yz}$ antibonding orbitals.

Before we conclude this analysis of D_{exp}, two additional contributions to D must be included. Once anisotropic covalency in the σ antibonding orbitals is introduced, it is no longer strictly correct to neglect the contribution from $^4T_1{}^b$. When the same procedure used to obtain eq 13 is employed, the following expressions for the spin–orbit coupling matrix elements between the ground state and the strong-field $^4T_1{}^b$ are obtained:

$$\langle {}^3/_2T_1{}^b z||H_{so}||{}^5/_2A_1\rangle = -18^{1/2}(1-\gamma^2)\zeta_{Fe^{3+}} \quad (15a)$$

$$\langle {}^3/_2T_1{}^b x,y||H_{so}||{}^5/_2A_1\rangle = -18^{1/2}(1-\gamma^2)^{1/2}(1-\beta^2)^{1/2}\zeta_{Fe^{3+}} \quad (15b)$$

Because π bonding contributions have been neglected in the t_2 antibonding orbitals, there is no ligand contribution to spin–orbit coupling. The energy (25 586 cm^{-1}) of the second $^4T_1$ was estimated from a ligand field analysis (vide infra). When the mixing coefficients found above are inserted, $D(^4T_1{}^b) = 0.03$ cm^{-1}.

With inclusion of covalency it also becomes necessary to consider the possibility that charge-transfer states can spin–orbit couple to the ground state and thereby contribute to D. By group theory, the only CT states that can spin–orbit couple to $^6A_1$ are $^6T_1$ states. In T_d symmetry the ligand LCAO's span the representations $t_1(nb)$, $t_2(\pi)$, $e(\pi)$, $t_2(\sigma)$, and $a_1(\sigma)$. These give rise to seven possible ligand to metal $^6T_1$ charge-transfer states, corresponding to the following one-electron transitions: $t_1(nb) \rightarrow e$, $t_1(nb) \rightarrow t_2$, $t_2(\pi) \rightarrow t_2$, $t_2(\pi) \rightarrow e$, $e(\pi) \rightarrow t_2$, $t_2(\sigma) \rightarrow t_2$, and $t_2(\sigma) \rightarrow e$. Two of these states ($^6T_1(t_1(nb) \rightarrow e)$ and $^6T_1(t_2(\pi) \rightarrow e)$) will have vanishingly small spin–orbit coupling to the ground state, and their contribution to D can be neglected. The contribution to D arising from any $^6T_1$ state is given by

$$D(^6T_1) = (2/315)[|\langle {}^5/_2T_1 x,y||H_{so}||{}^5/_2A_1\rangle|^2/E_{x,y} - |\langle {}^5/_2T_1 z||H_{so}||{}^5/_2A_1\rangle|^2/E_z] \quad (16)$$

With use of the same procedure as for the $^4T_1$ states, the following expressions for spin–orbit coupling between the low-symmetry components of the five contributing $^6T_1$ states and the ground state are derived:

$$\langle {}^5/_2T_1(t_1(nb) \rightarrow t_2)x,y||H_{so}||{}^5/_2A_1\rangle = -({}^7/_{40})^{1/2}(\gamma+\beta)\zeta_{Cl^-} \quad (17a)$$

$$\langle {}^5/_2T_1(t_1(nb) \rightarrow t_2)z||H_{so}||{}^5/_2A_1\rangle = -({}^7/_{10})^{1/2}\gamma\zeta_{Cl^-} \quad (17b)$$

$$\langle {}^5/_2T_1(t_2(\pi) \rightarrow t_2)x,y||H_{so}||{}^5/_2A_1\rangle = -i({}^{21}/_{40})^{1/2}(\gamma+\beta)\zeta_{Cl^-} \quad (17c)$$

$$\langle {}^5/_2T_1(t_2(\pi) \rightarrow t_2)z||H_{so}||{}^5/_2A_1\rangle = -i({}^{21}/_{10})^{1/2}\gamma\zeta_{Cl^-} \quad (17d)$$

$$\langle {}^5/_2T_1(e(\pi) \rightarrow t_2)x,y||H_{so}||{}^5/_2A_1\rangle = 6({}^7/_{10})^{1/2}[\alpha(1-\gamma^2)^{1/2}\zeta_{Fe^{3+}} - i({}^1/_6)^{1/2}\gamma(1-\alpha^2)^{1/2}\zeta_{Cl^-}] \quad (17e)$$

$$\langle {}^5/_2T_1(e(\pi) \rightarrow t_2)z||H_{so}||{}^5/_2A_1\rangle = 6({}^7/_{10})^{1/2}[\alpha(1-\beta^2)^{1/2}\zeta_{Fe^{3+}} - i({}^1/_6)^{1/2}\beta(1-\alpha^2)^{1/2}\zeta_{Cl^-}] \quad (17f)$$

$$\langle {}^5/_2T_1(t_2(\sigma) \rightarrow e)x,y||H_{so}||{}^5/_2A_1\rangle = 6({}^7/_{10})^{1/2}[\gamma(1-\alpha^2)^{1/2}\zeta_{Fe^{3+}} - i({}^1/_6)^{1/2}\alpha(1-\gamma^2)^{1/2}\zeta_{Cl^-}] \quad (17g)$$

$$\langle {}^5/_2T_1(t_2(\sigma) \rightarrow e)z||H_{so}||{}^5/_2A_1\rangle = 6({}^7/_{10})^{1/2}[\beta(1-\alpha^2)^{1/2}\zeta_{Fe^{3+}} - i({}^1/_6)^{1/2}\alpha(1-\beta^2)^{1/2}\zeta_{Cl^-}] \quad (17h)$$

$$\langle {}^5/_2T_1(t_2(\sigma) \rightarrow t_2)x,y||H_{so}||{}^5/_2A_1\rangle = ({}^{63}/_{20})^{1/2}[\beta(1-\gamma^2)^{1/2} + \gamma(1-\beta^2)^{1/2}]\zeta_{Fe^{3+}} \quad (17i)$$

$$\langle {}^5/_2T_1(t_2(\sigma) \rightarrow t_2)z||H_{so}||{}^5/_2A_1\rangle = ({}^{63}/_5)^{1/2}[\gamma(1-\gamma^2)^{1/2}]\zeta_{Fe^{3+}} \quad (17j)$$

As with the $^4T_1$ states the matrix elements are indexed according to their T_d parent, and in addition these matrix elements are indexed according to the one-electron transition which gives rise to that state. A quantitative evaluation of the charge-transfer contribution to D requires an estimate of the $^6T_1$ energy denominators in eq 16. These are estimated to be 33 000 cm^{-1} on the basis of the energies of the observed electric dipole allowed $^6A_1 \rightarrow {}^6T_2$ transitions (Figure 12). The low-symmetry splitting of the charge-transfer states should be very small and thus is approximated to be zero. This is experimentally supported by the lack of low-symmetry splitting observed in the $^6T_2$ charge-transfer state (Figure 12).

If we now consider all the contributions to D and fit $\beta^2 - \gamma^2$ to D_{exp}, $\beta^2 - \gamma^2 = 0.05$ is required. The final set of mixing coefficients are $\alpha^2 = 0.16$, $\beta^2 = 0.305$, and $\gamma^2 = 0.255$. The individual contributions to D are 0.08 cm^{-1} ($^4T_1{}^a$), 0.03 cm^{-1} ($^4T_1{}^b$), –0.10 cm^{-1} ($^4T_1{}^c$), and –0.05 cm^{-1} for the combined $^6T_1$ states.

An independent probe of spin–orbit coupling between the ground state and the $^6T_1$ charge-transfer states comes from a quantitative analysis of the ground-state g values. The deviation of the g values from 2.0023 arises from spin–orbit coupling between the $^6A_1$ ground state and T_1 states of the same spin. These are the same states that give rise to the charge-transfer contribution to D. With use of the irreducible tensor method the following expressions for the contribution to the g shift from spin–orbit coupling between $^6T_1$ charge-transfer states and the ground state are derived:

$$\Delta g_z = 4(\langle {}^5/_2T_1 z||H_{so}||{}^5/_2A_1\rangle\langle {}^5/_2T_1 z||L||{}^5/_2A_1\rangle)/E_z(1890)^{1/2} \quad (18a)$$

$$\Delta g_{x,y} = 4(\langle {}^5/_2T_1 x,y||H_{so}||{}^5/_2A_1\rangle\langle {}^5/_2T_1 x,y||L||{}^5/_2A_1\rangle)/E_{x,y}(1890)^{1/2} \quad (18b)$$

With use of eq 17 and the mixing coefficients found above to evaluate the spin–orbit and angular momentum matrix elements required in eq 18, $\Delta g_z = 0.011$ and $\Delta g_{x,y} = 0.010$. These values are close to the experimental values of 0.012 and 0.010. The fact that the spin–orbit coupling analysis can also explain the g-value deviations indicates that the model is internally consistent.

Further, because the g-value deviations and the charge-transfer contribution to D arise from the same spin–orbit interaction, it is possible to relate the two effects. With use of eq 16 and 18

(27) Butcher, K. D.; Didziulis, S. V.; Solomon, E. I. To be submitted for publication.

and the approximation that $\langle {}^5/_2T_1||L||{}^5/_2A_1\rangle = ({}^{10}/_{21})^{1/2}\cdot\langle {}^5/_2T_1||H_{so}||{}^5/_2A_1\rangle/(\bar{\zeta})$ the following expression relating the anisotropy in the experimental g values to the total charge-transfer contribution to D is obtained:

$$D({}^6T_1) = (\bar{\zeta}/10)(g_{x,y} - g_z) \qquad (19)$$

$\bar{\zeta}$ is an effective spin–orbit coupling constant, which includes metal and ligand contributions. It is reasonable to approximate $\bar{\zeta}$ as the average between the Fe^{3+} (430 cm^{-1}) and the ligand (580 $cm^{-1}/6^{1/2}$) spin–orbit coupling constants, giving $\bar{\zeta} \approx 350$ cm^{-1}. The ligand spin–orbit coupling constant is reduced by $6^{1/2}$ due to geometrical considerations and the difference between p and d orbitals (i.e. $l = 1$ versus $l = 2$). With use of eq 19, a spin–orbit coupling constant of 350 cm^{-1}, and the experimental g values the charge-transfer contribution to D is estimated to be −0.07 cm^{-1}, while our earlier calculation predicted a similar value of −0.05 cm^{-1}. Thus, one can use eq 19 to directly obtain an estimate of the charge-transfer contribution to D without the necessity of deriving the expressions in eq 17. This is important because it becomes increasingly difficult to derive accurate expressions for spin–orbit coupling between the ground and excited charge-transfer states as the symmetry is lowered or when the ligand is polyatomic as is the case for thiolates. For these complexes too many approximations must be made to obtain expressions parallel to those of eq 17, and thus the charge-transfer contribution to D is best determined experimentally through the use of eq 19.

C. Ligand Field Analysis. The energies of the observed ^{4}h LF states (Table IV) were fit to the Tanabe–Sugano matrices by using a nonlinear fitting routine.[28] The values obtained for the ligand field parameters are $Dq = 655 \pm 213$ cm^{-1}, $B = 444 \pm 239$ cm^{-1}, and $C = 2728 \pm 700$ cm^{-1}. The calculated energies of the ^{4}h states are compared to the experimental energies in Table IV. Note that the large standard deviation in the calculated parameters reflects the rather large deviation of the calculated energies from experimental energies for the two highest excited states, $^4T_2{}^b$ and $^4E^b$. Trees'[29] atomic correction is found to alter only slightly the values for B and C but not to change the quality of the fit for the $^4T_2{}^b$ and $^4E^b$ states.

The electron repulsion parameters B and C for ferric tetrachloride are greatly reduced from the free ion values[30] of $B = 1100$ cm^{-1} and $C = 3750$ cm^{-1}. This strong reduction of electron repulsion parameters is also clearly seen in the energy of the LF-independent $^4E^a$ state, which depends only upon electron repulsion terms. Experimentally this is found to occur at only 56% of the energy of the free ion ^{4}G term (32 290 cm^{-1}). Similarly, the $^4E^b$ state is found at 58% of the energy of the free ion ^{4}D term (38 880 cm^{-1}) to which it correlates.

The low-symmetry splittings within the $^4T_1{}^a$ and $^4T_2{}^a$ states may be further analyzed to obtain the experimental energy ordering of the one-electron antibonding "d" orbitals. With use of the irreducible tensor method, the low-symmetry splittings of the many-electron states in the strong-field limit are factored in terms of the splittings of the constituent one-electron orbitals:[31]

$$\Delta^1T_1(t_2{}^4e^1) = -\Delta^4T_1(t_2{}^2e^3) = \delta + {}^3/_4\mu$$

$$\Delta^4T_2(t_2{}^4e^1) = -\Delta^4T_2(t_2{}^2e^3) = \delta - {}^3/_4\mu$$

$$\Delta^4T_2(t_2{}^3e^2) = \Delta^4T_2(t_2{}^3e^2) = 0 \qquad (20)$$

Here δ is the energy separation between $d_{xz,yz}$ and d_{xy} and μ is the separation between $d_{x^2-y^2}$ and d_{z^2}. The low-symmetry splitting Δ^4T_i is defined to be positive if $^4T_i z$ is lowest. It is also necessary to obtain the linear combinations of strong-field configurations that make up the $^4T_1{}^a$ and $^4T_2{}^a$ states. This is accomplished by diagonalizing the Tanabe–Sugano matrices with use of the best-fit LF parameters given above:

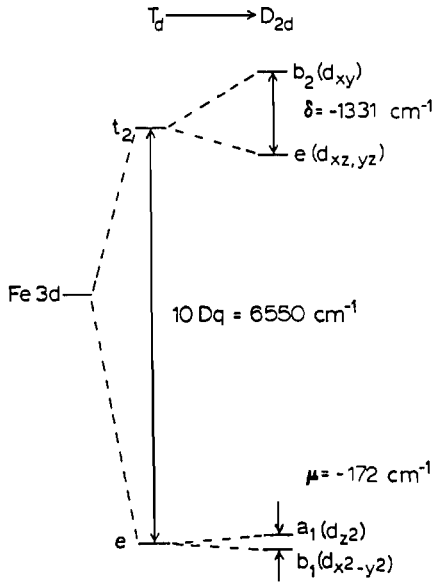

Figure 13. One-electron "d" orbital splitting pattern for D_{2d} $FeCl_4^-$ at 5 K.

$$^4T_1{}^a = (0.978)^4T_1(t_2{}^2e^3) + (0.108)^4T_1(t_2{}^3e^2) - (0.179)^4T_1(t_2{}^4e^1)$$

$$^4T_2{}^a = (0.885)^4T_2(t_2{}^2e^3) - (0.362)^4T_2(t_2{}^3e^2) - (0.292)^4T_2(t_2{}^4e^1) \qquad (21)$$

When these results are combined with eq 20, the values obtained for the one-electron splittings are $\delta = -1331$ cm^{-1} and $\mu = -172$ cm^{-1}. These one-electron splittings are shown in Figure 13. This ordering is consistent with the anisotropies in covalency deduced from the ZFS analysis. The finding of d_{xy} highest in energy indicates that it has a stronger covalent antibonding interaction with the ligands than do the $d_{xz,yz}$ orbitals. The e set of orbitals are found to be lowest in energy and not strongly split by the D_{2d} crystal field, which supports the approximation in the preceding section concerning the assignment of the same mixing coefficients to both d_{z^2} and $d_{x^2-y^2}$.

Discussion

The present study generates an experimental assignment of the LF spectra of high-spin ferric complexes using magnetooptical techniques. A key feature of these experiments is the use of high magnetic field and low temperature to populate only the $M = -{}^5/_2$ sublevel of the ground state. The marked dependence of polarized intensity upon ground spin state is due to the involvement of spin as well as orbital vector coupling coefficients in the selection rules derived for the spin–orbit intensity-gaining mechanism. This approach affords detailed assignments of the low-symmetry fine structure in the $^4T_1{}^a$ and $^4T_2{}^a$ region. The E,F band system thought to be the degenerate $^4A_1$–$^4E^a$ transitions[8] is now assigned as $^4E^a$ and $^4T_2{}^b$, and band G is unambiguously assigned as the $^4E^b$ transition.

With the experimental energies of the $^4T_1{}^a$ low-symmetry components, it is found that Griffith's model (eq 11) for the origin of ZFS produces a calculated D which is opposite in sign to that of the experimental D. This has required a major modification of Griffith's theory to include the effects of anisotropic covalency upon the spin–orbit coupling matrix elements. In the Griffith model, the sign of D is determined by the energy ordering of the $^4T_1$ low-symmetry components since the model assumes that $\langle {}^3/_2T_1x,y||H_{so}||{}^5/_2A_1\rangle = \langle {}^5/_2T_1z||H_{so}||{}^5/_2A_1\rangle$ in eq 10. However, the experimental sign of D indicates that $\langle {}^3/_2T_1x,y||H_{so}||{}^5/_2A_1\rangle$ is greater than $\langle {}^3/_2T_1z||H_{so}||{}^5/_2A_1\rangle$ in D_{2d} $FeCl_4^-$. This inequality results in a quenching of the positive $^4T_1{}^a$ contribution to D but an enhancement of the negative $^4T_1{}^c$ contribution. The net effect drives D in the opposite direction relative to the predictions of the

(28) Johnson, K. J. *Numerical Methods in Chemistry*; Marcel Dekker: New York, 1980.
(29) Stevenson, R. *Multiplet Structures of Atoms and Molecules*; W. B. Saunders: Philadelphia, 1965.
(30) Reader, J.; Sugar, J. *J. Phys. Chem. Ref. Data* **1975**, *4*, 397.
(31) Goode, D. H. *J. Chem. Phys.* **1965**, *43*, 2883.

Griffith model (eq 11). The inequivalence of these D_{2d} reduced matrix elements is caused by anisotropy in covalency in less than cubic symmetry. When covalent one-electron antibonding orbitals are used to evaluate these reduced matrix elements (eq 13), it is found that the empirically deduced inequality results if the coefficient of covalent mixing for the d_{xy} orbital is greater than that for $d_{xz,yz}$.

Contributions to D in addition to those from $^4T_1{}^{a,c}$ states arise once anisotropic covalency is included in the model. These contributions derive from $^6T_1$ CT states and the $^4T_1{}^b$ LF state. In the $FeCl_4^-$ complex these contributions individually have non-negligible contributions to D, but the net contribution is small because they oppose each other. The charge-transfer contribution to D is the hardest to obtain because the energies for the states involved must be estimated and because deriving accurate expressions for the SO matrix elements between CT states and the ground state is difficult. Alternatively, the total CT contribution may be estimated experimentally through the use of eq 19 if the g values can be accurately determined. This method should be generally used to estimate the CT contribution to D in systems with low-lying CT states that are strongly low-symmetry-split as is the case for ferric tetrathiolate complexes such as rubredoxin. It is also likely that high-spin ferric heme systems will show a large charge-transfer contribution to D.

Further analysis of the $^4T_1{}^a$ and $^4T_2{}^a$ low-symmetry splittings provides an energy ordering of the one-electron orbitals. It is found that the d_{xy} antibonding orbital is 1300 cm^{-1} above the $d_{xz,yz}$ antibonding orbitals. This is consistent with the compressed D_{2d} geometry of the $FeCl_4^-$ complex, which shifts the ligand p–σ bonding orbitals toward the xy plane and away from the xz and yz planes. This is also consistent with the analysis of the sign of D, which leads to the conclusion that the d_{xy} orbital is more covalent than the $d_{xz,yz}$ orbitals. It should be emphasized that the order of the $^4T_1$ low-symmetry splitting and the anisotropy in covalency are coupled since they both derive from the low-symmetry splitting of the t_2 orbitals (which are σ antibonding in T_d), and thus this effect will always quench the $^4T_1{}^a$ contribution to D in distorted T_d high-spin d^5 complexes.

The final application of the experimental band assignments has been to evaluate the ability of the three-parameter ligand field theory to account for the observed energies. This theory has been remarkably successful when applied to high-spin ions of the first-row transition metals in the +2 oxidation state. But here the spectral fit is not very good, particularly for the higher energy $^4T_2{}^b$ and $^4E^b$ states. Such deviations from the predictions of ligand field theory can also be found in other compounds in the +3 oxidation state (for example, CrX_6^{3-}; X = Cl, Br).[32] These difficulties appear to result from the fact that the electron repulsion parameters appropriate for the free ion do not carry over to molecular symmetry when covalency is significant and that the covalent interactions are stronger in compounds of metal ions in higher oxidation states. Bird and Day[33] have given a more general group theory treatment for electron repulsion in molecular symmetry, but there are too many parameters to evaluate (17 for tetragonal symmetry). That covalency is particularly strong in high-spin d^5 Fe^{3+} is suggested by the very large central field reduction in electron repulsion energies (nephelauxetic effect).[34] In particular, the $^4E^a$ energy which depends only on electron repulsion terms is only 56% of the energy of the ^4G free ion term, whereas in the isoelectronic $MnCl_4^{2-}$ this state occurs at 86% of the ^4G energy.[35] Unfortunately, there are no theoretical treatments that directly relate coefficients of covalent mixing to the reduction of electron repulsion terms. A second possible source of the significant deviations from the Tanabe–Sugano theory could be spin polarization effects on the antibonding wave functions, which would be larger in a high-spin d^5 ion due to electron exchange interactions. An alternate approach toward describing the bonding in Fe(III) compounds now being pursued is to calibrate Xα–SW calculations[27] by using the detailed information on the ground and excited states provided by the present spectral study. In particular, the sphere size parameter can be adjusted in these calculations to fit the excited-state transition energies and thus get an experimentally calibrated estimate of the bonding parameters. These calculations should also provide significant insight into the effects of spin polarization on the description of bonding in high-spin d^5 complexes. We anticipate reporting the results of these calculations and their correlation to variable-energy photoelectron spectra in the near future.[27]

Acknowledgment. We thank the National Science Foundation (Grant No. CHE-8613376) for support of this research. M.S.G. and J.C.D. acknowledge the NSF for graduate research fellowships.

(32) (a) Wood, D. L.; Ferguson, J.; Knox, K.; Dillon, J. F., Jr. *J. Chem. Phys.* **1963**, *39*, 890. (b) Ferguson, J.; Wood, D. L. *Aust. J. Chem.* **1970**, *23*, 861.
(33) Bird, B. D.; Cooke, E. A.; Day, P.; Orchard, A. F. *Philos. Trans. R. Soc. London, A* **1974**, *276*, 278.
(34) Jørgensen, C. K. *Discuss. Faraday Soc.* **1958**, *26*, 110.
(35) Jørgensen, C. K. *Prog. Inorg. Chem.* **1962**, *4*, 73.

Contribution No. 7809 from the Arthur Amos Noyes Laboratory, California Institute of Technology, Pasadena, California 91125

Excited-State Properties of Dioxorhenium(V). Generation and Reactivity of Dioxorhenium(VI)

H. Holden Thorp, J. Van Houten,† and Harry B. Gray*

Received October 17, 1988

The excited-state properties of *trans*-$ReO_2(py)_4^+$ (ReO_2^+) in acetonitrile solution have been investigated. The excited-state absorption spectrum of ReO_2^+ is dominated by bleaching of the ground-state MLCT ($(d_{xy})^2 \rightarrow (d_{xy})^1(\pi^*(py))^1$) and d–d ($(d_{xy})^2 \rightarrow (d_{xy})^1(d_{xz},d_{yz})^1$) systems. A weak excited-state absorption at ~500 nm is assigned to $(d_{xy})^1(d_{xz},d_{yz})^1 \rightarrow (d_{xz},d_{yz})^2$. The reduction potential of $ReO_2^{2+/+*}$ is estimated from emission and electrochemical data to be –0.7 V (SSCE). The ReO_2^+ excited state efficiently ($k_f = 3.6 \times 10^8$ M^{-1} s^{-1}) reduces methylviologen and other pyridinium and olefin acceptors. The recombination electron-transfer reaction is diffusion-controlled ($k_b = 2.1 \times 10^{10}$ M^{-1} s^{-1}). The Re(VI) species ReO_2^{2+}, which can be generated photochemically or electrochemically, is a powerful oxidant. Secondary alcohols and silanes are readily oxidized by ReO_2^{2+}. Acetophenone is the product of *sec*-phenethyl alcohol oxidation.

Introduction

Transition-metal complexes whose excited states undergo electron transfer to form oxidants are under intense study.[1-5] Our recent work in this area has centered on *trans*-$ReO_2(py)_4^+$ (ReO_2^+; py = pyridine) whose lowest excited state (^3E_g) is long-lived (τ

† Department of Chemistry, St. Michael's College, Winooski, VT 05404.

(1) (a) Kalyanasundaram, K. *Coord. Chem. Rev.* **1982**, *46*, 159. (b) Meyer, T. J. *Pure Appl. Chem.* **1986**, *58*, 1193. (c) Krause, R. A. *Struct. Bonding* **1987**, *67*, 1.

0020-1669/89/1328-0889$01.50/0